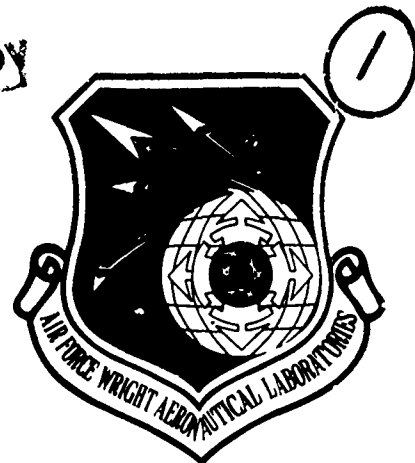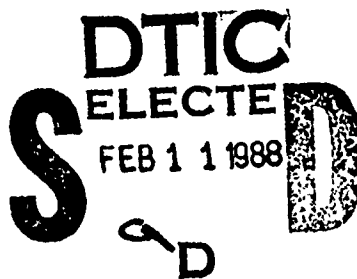AFWAL-TR-87-3031

DTIC FILE COPY

MODELING TECHNIQUES FOR COMPOSITES SUBJECTED
TO RAPID THERMAL PULSE LOADING

A. C. Mueller

FLOW RESEARCH COMPANY
21414 68TH AVENUE SOUTH
KENT, WASHINGTON 98032

DTIC
SELECTED
FEB 1 1 1988
D

FEBRUARY 1987

FINAL REPORT FOR PERIOD JULY 1986 - FEBRUARY 1987

APPROVED FOR PUBLIC RELEASE; DISTRIBUTION UNLIMITED.

FLIGHT DYNAMICS LABORATORY
AIR FORCE WRIGHT AERONAUTICAL LABORATORIES
AIR FORCE SYSTEMS COMMAND
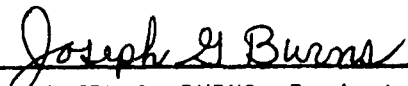WRIGHT-PATTERSON AIR FORCE BASE, OHIO 45433-6553

AD-A190 997

88 2 08 099

NOTICE

When Government drawings, specifications, or other data are used for any purpose other than in connection with a definitely related Government procurement operation, the United States Government thereby incurs no responsibility nor any obligation whatsoever; and the fact that the government may have formulated, furnished, or in any way supplied the said drawings, specifications, or other data, is not to be regarded by implication or otherwise as in any manner licensing the holder or any other person or corporation, or conveying any rights or permission to manufacture use, or sell any patented invention that may in any way be related thereto.

This report has been reviewed by the Office of Public Affairs (ASD/PA) and is releasable to the National Technical Information Service (NTIS). At NTIS, it will be available to the general public, including foreign nations.

This technical report has been reviewed and is approved for publication.

JOSEPH G. BURNS, Project Engr
Fatigue, Fracture & Reliability Gp
Structural Integrity Branch

FRANK D. ADAMS, Chief
Structural Integrity Branch
Structures Division

FOR THE COMMANDER

HENRY A. BONDARUK, JR, Colonel, USAF
Chief, Structures Division

If your address has changed, if you wish to be removed from our mailing list, or if the addressee is no longer employed by your organization please notify AFWAL/F&&&, *W-PAFB, OH 45433 to help us maintain a current mailing list.*

Copies of this report should not be returned unless return is required by security considerations, contractual obligations, or notice on a specific document.

REPORT DOCUMENTATION PAGE

Form Approved
OMB No. 0704-0188

1a. REPORT SECURITY CLASSIFICATION	1b. RESTRICTIVE MARKINGS
Unclassified	

2a. SECURITY CLASSIFICATION AUTHORITY	3. DISTRIBUTION / AVAILABILITY OF REPORT
	Approved for public release; distribution unlimited
2b. DECLASSIFICATION / DOWNGRADING SCHEDULE	

4. PERFORMING ORGANIZATION REPORT NUMBER(S)	5. MONITORING ORGANIZATION REPORT NUMBER(S)
Flow Research Report No. 392 TR-392/02-87	AFWAL-TR-87-3031

6a. NAME OF PERFORMING ORGANIZATION	6b. OFFICE SYMBOL (If applicable)	7a. NAME OF MONITORING ORGANIZATION
Flow Research Company		AF Wright Aeronautical Laboratories Flight Dynamics Laboratory (AFWAL/FIBEC)

6c. ADDRESS (City, State, and ZIP Code)	7b. ADDRESS (City, State, and ZIP Code)
21414 68th Avenue South Kent WA 98032	Wright-Patterson AFB OH 45433-6553

8a. NAME OF FUNDING / SPONSORING ORGANIZATION	8b. OFFICE SYMBOL (If applicable)	9. PROCUREMENT INSTRUMENT IDENTIFICATION NUMBER
DOD SBIR Program Office		F33615-86-C-3226

8c. ADDRESS (City, State, and ZIP Code)	10. SOURCE OF FUNDING NUMBERS			
	PROGRAM ELEMENT NO.	PROJECT NO.	TASK NO	WORK UNIT ACCESSION NO.
Washington DC 20301	65502F	3005	30	52

11. TITLE (Include Security Classification)

Modeling Techniques for Composites Subjected to Rapid Thermal Pulse Loading

12. PERSONAL AUTHOR(S)
A.C. Mueller, K.Y. Lin, K.A. Holsapple

13a. TYPE OF REPORT	13b. TIME COVERED	14. DATE OF REPORT (Year, Month, Day)	15. PAGE COUNT
Final	FROM 8607 TO 8702	1987 February	55

16. SUPPLEMENTARY NOTATION

17.	COSATI CODES		18 SUBJECT TERMS (Continue on reverse if necessary and identify by block number)
FIELD	GROUP	SUB-GROUP	composite materials, delaminations, finite element methods, strategic defense initiative, fracture mechanics, stress intensity factors, pulse heating, stress waves
11	04		
20	05		

19. ABSTRACT (Continue on reverse if necessary and identify by block number)

Composite structures may be subjected to sources of thermal energy including X-rays from nuclear weapons, lasers, and particle beams. This study addresses the need for analysis tools to predict the effects of rapid thermal pulse loading on aerospace composite materials that contain delaminations. A major objective of this study is to determine the feasibility of providing such an engineering design tool. Existing codes have been modified to analyze the stress wave generation and its subsequent interaction with a delamination. The finite difference model for simulation of the stress wave initiation includes the thermomechanical coupling and a general equation of state model to account for phase changes. A singular finite element model is employed to account for the stress singularity near a delamination within the anisotropic composite plies. Tests have been conducted to ensure that the singular element is applicable to the present problem. (Keywords)

(continued on reverse)

20. DISTRIBUTION / AVAILABILITY OF ABSTRACT	21. ABSTRACT SECURITY CLASSIFICATION
☒ UNCLASSIFIED/UNLIMITED ☐ SAME AS RPT. ☐ DTIC USERS	Unclassified

22a. NAME OF RESPONSIBLE INDIVIDUAL	22b. TELEPHONE (Include Area Code)	22c. OFFICE SYMBOL
Joseph G. Burns	(513) 255-6104	AFWAL/FIBEC

DD Form 1473, JUN 86   Previous editions are obsolete.   SECURITY CLASSIFICATION OF THIS PAGE

19. ABSTRACT (continued)

The results of the stress wave generation show that the ensuing wave will have both compressive and tensile parts, with the magnitude of the compressive part dependent on the deposition energy density and the magnitude of the tensile part dependent on the fracture toughness of the surface plies.

The spalling event, as the stress wave reflects from the back surface and interacts with an existing delamination, was also modeled. The analysis shows that the strain energy release rate is insensitive to ply stacking for waves in pure tension but is very sensitive for shear wave interaction. The ambient temperature of the plate also plays an important role in the fracture because of thermal stresses resulting from curing. Pre- and postprocessors, used to generate the mesh, assign material properties, and display the results, proved valuable. It is anticipated that the proposed work would lead to the development of an engineering design tool to evaluate the vulnerability of composite aerospace structures to energetic rapid thermal loading. The code can be an integral part of a basic research effort to develop improved material design concepts for shock wave damage mitigation.

TABLE OF CONTENTS

LIST OF FIGURES

LIST OF TABLES

1. INTRODUCTION

The physical problem we are addressing in this study is the rapid deposition of thermal energy on the surface of a composite plate within which a delamination exists. The high energy flux will stress and perhaps vaporize the surface plies, and a shock stress wave is initiated through thermal expansion and the momentum imparted by the blowoff. As this compressive wave initially passes the delamination, the crack will tend to close and the wave will simply pass through. But as the wave reflects off the bottom free surface, it will return as a tensile wave. This wave will open the delamination and produce excessive stresses at the crack tip. The high stress field could conceivably cause the delamination to grow and result in the catastrophic failure of the plate. In addition to the initiation of a longitudinal stress wave, a shear wave may ensue from a nonuniform spatial distribution or edge effects of the laser energy flux. Matters are further complicated by the anisotropic and nonhomogeneous makeup of the composite plate. Hence, the longitudinal and shear waves will propagate at speeds dependent on the ply orientation.

Several time scales may be identified. The energy deposition typically occurs within hundredths of a microsecond. Depending on the wavelength of the source, the energy may be deposited on just the surface or throughout the plate, but in either case it results in an almost instantaneous change in the temperature. This rapid rise in temperature may produce a phase change at the surface. Subsequently, the pressure in the gas phase becomes very high, and the adjacent solid portion responds with a stress wave. This wave will traverse the thickness of the plate on the order microseconds. The conduction of heat takes place over a much longer time scale. For example, a temperature change of 1% requires on the order of 100 milliseconds.

1.1 The Energy Deposition Phase

The analysis tools required for the study of composite structures subjected to rapid thermal pulses are conveniently considered in three parts, two of which are analyzed in some detail in this study. The first part is the determination of the nature of the thermal pulse from knowledge or assumptions about the source of that pulse, which is only discussed in generalities here. Sources of interest include laser weapons, nuclear weapon X-rays, particle beams, and other energy sources. The analysis of this part of the problem must consider the interaction of an electromagnetic source with the material

1

of the composite structure and must analyze the subsequent radiation transport in that material. Analysis techniques are available, but experimental data sufficient to define material properties for energy deposition in polymeric materials characteristic of composites are sparse or nonexistent.

The outcome of a study of this radiation transport is a time-position profile of the thermodynamic state of the composite structure. Fortunately, to study and develop the tools required for the remaining two parts of the problem, it is not necessary to have specific numerical results. Rather, it is only necessary to know the general nature of the results so that the tools for the rest of the analysis are sufficient to cope with the range of possibilities. A short discussion of the general nature, and of the differences due to the variety of possible source types, is given.

It is convenient to classify energy sources according to their range of initial spatial influence and their temporal duration. The best studied source is the detonation of a nuclear weapon near a structure of interest. The predominant energy of a modern fusion device is in a substantial X-ray output that impinges on, and is absorbed into, the adjacent material. If the detonation is in the atmosphere, the surrounding air absorbs the energy, and a blast wave is formed that propagates outward and strikes nearby structures. Alternatively (and exclusively if there is no significant atmosphere present), the radiation directly reaches a nearby structure. The energy is then absorbed by the material in the structure.

The time scales of this energy transport phase are typically very short in comparison to the other significant time scales of the problem. In many cases, it is considered instantaneous. The characteristic depth of the energy deposition depends markedly on the composition of the structure. Materials with high atomic numbers absorb the energy in very shallow depths, while so-called "low-Z" materials have much greater absorption depths.

Thus, energy deposition due to nuclear devices is typically of very short duration. The depths of deposition can be either thin compared to structural dimensions (e.g., a skin thickness of a missile) or of that same size.

When considering laser weapons, there are important differences in this picture due to the longer wavelengths of the radiation. The time scales, for a single pulse, are still short. However, the deposition thickness is very small and, as a result of the very high energy densities, it will vaporize and "blow off" on a short time scale, which can have a significant quenching effect

on the energy deposition itself. In this case, there can be important inter-
actions between the thermodynamics of the material, the resulting wave actions,
and the energy deposition itself. For that reason, multiple and rapidly pulsed
weapon outputs are under consideration. The tools to be developed here must
be able to handle this important case.

1.2 The Initial Thermodynamic State

The result of an analysis of the energy deposition and radiation transport
is a specified physical state for all material points in the structure as a
function of time. As was discussed, the time scale of this phase of the
problem is typically very short and, for the present, will be considered to be
instantaneous.

The "physical state" means the thermodynamic state. The nature of this
state can be described by referral to a typical phase-state diagram for a
material. Figure 1 shows a typical temperature-density plot of all equilibrium
thermodynamic states for a metal. The boundaries between the solid, liquid,
and vapor phases are shown. Also shown is the locus, of points at a constant
one-atmosphere pressure. Along that locus, the melt and vapor points are iden-
tified. The critical point and triple line are also indicated.

Only certain parts of this diagram are of importance to the present
analysis. A typical material point is initially at standard temperature and
pressure. For clarity, Figure 2 will be used for this discussion; this
initial point is labeled as point A.

For instantaneous energy deposition, the temperature (and also the internal
energy) is suddenly increased. Since there is insufficient time for material
motions, the material will remain at constant mass density. Consequently, the
material point will achieve the state at point B, a point directly above point
A. Depending on the magnitude of the energy absorbed, this point can be well
into the liquid or vapor regions. However, since the mass density remains at
the initial value, the pressure will be very high. As an example, point B is
shown along a one-megabar pressure line, corresponding to a point typically
well above the critical point.

We will discuss in detail the subsequent material motions and wave propaga-
tions that result from such initial states throughout a structure. A material
point will not remain at point B, but the material will expand and the pressure

3

will reduce eventually back to normal pressure. Since these motions occur after the energy deposition, they are adiabatic and, as a consequence, the path followed in this thermodynamic phase space is along an isentrope. A typical isentrope from point B is indicated. The one shown happens to intersect the vapor-liquid dome, but it will not if point B is at a sufficiently high temperature. The final states of the material will ultimately be at very low densities, and the material will be hot and expanded.

This discussion serves to identify the thermodynamic description and model that is needed for the initial deposition phase for an analysis of the type studied here. A relatively precise description of all states at nominal and lower densities is needed. A model of the phase boundaries and the shape of the pressure curves and adiabats (isentropes) in this region is also needed.

Subsequent wave motions can introduce further states. In the case that a layer of surface material vaporizes and blows off at high velocity, or a thin layer of material is spalled off, then a shock wave will be generated that propagates into the interior of the structure. This shock wave is similar to one that would be generated by an impact at the surface. The resulting shocked states lie along a Hugoniot curve centered at the initial point of the material. A typical Hugoniot curve from the standard temperature and pressure is also shown in Figure 2. We can see that these states are at higher than normal density and temperature.

In the case of composite materials, specific data on these thermodynamic states are very sparse. In the present Phase I study, a thorough literature search has not been conducted, but preliminary investigations uncovered only a very few thermodynamic properties, including only the initial density, the Grüneisen parameter, the wave speed, and thermal expansion at standard temperature and pressure. No data were found on temperature states above a few hundred degrees, and none describing phase-change mechanisms. Clearly, before we can have sufficient confidence in energy deposition studies, much more work is needed in this area: both analytical descriptions of the thermodynamics of composite materials and experimental tests to verify and calibrate those analytical models. The additional features arising from the multiple-constituency of the composite materials will also require further investigation.
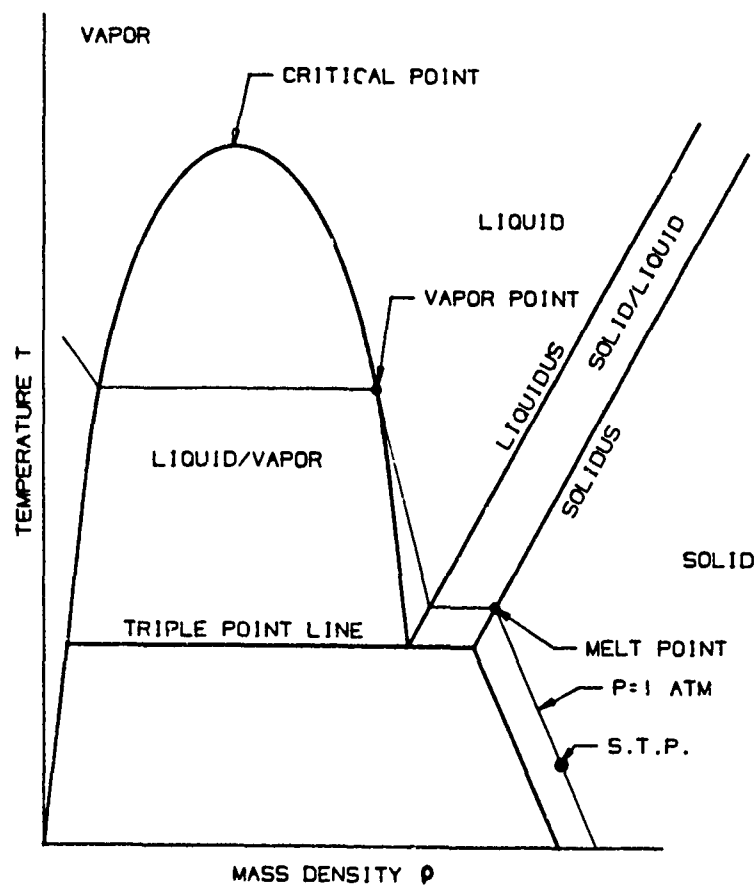
Figure 1. Phase Diagram for a Typical Metal
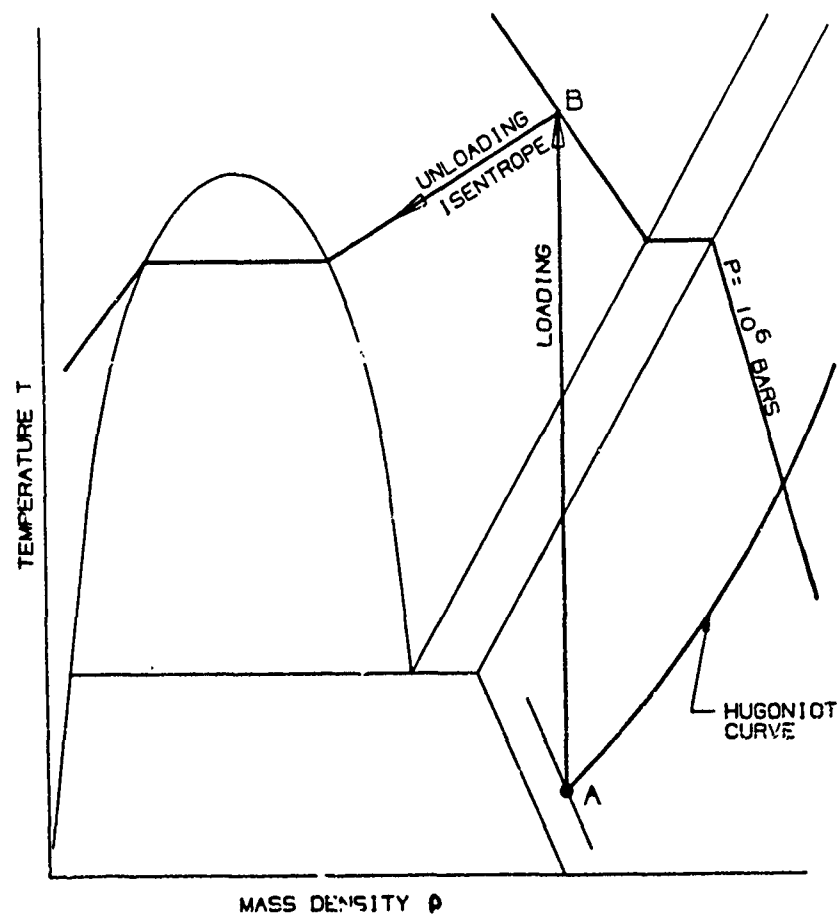
Figure 2. Typical Loading History

5

1.3 Typical Wave Profiles

To understand the computer results to be shown shortly, we first describe the general nature of the stress pulses that will arise in the cases of rapid thermal pulses. An idealized description is given here, followed by a presentation of some actual code output that includes all of the real physics of the problem.

For an idealized case, consider a plate of thickness t in the x direction. We may assume that there is an instantaneous triangular uniform energy deposition at the free surface of that plate, with the maximum value at the surface and dropping linearly to zero at some depth h less than t.

There is a resulting high pressure in that deposition region that produces an initial pressure profile as shown in sketch 1.

The general effect of this initial state can be understood by considering the special case of a linear elastic material for which superposition holds. In that case, the balance of linear momentum reduces to the well-known one-dimensional wave equation. If the pulse is not near the free surface, then the initial pulse shown above would split into two equal parts, one traveling to the right at the wave velocity c, and one to the left. Thus, a short instant Δt later, these two waves look as shown in sketch 2. However, there is a free surface at x = 0 to consider. The condition that the pressure be zero at x = 0 is satisfied by adding a third wave, opposite to

6
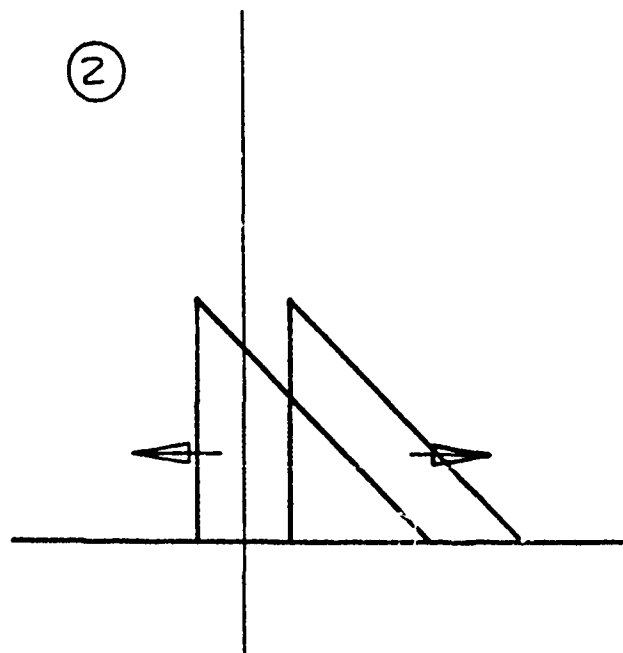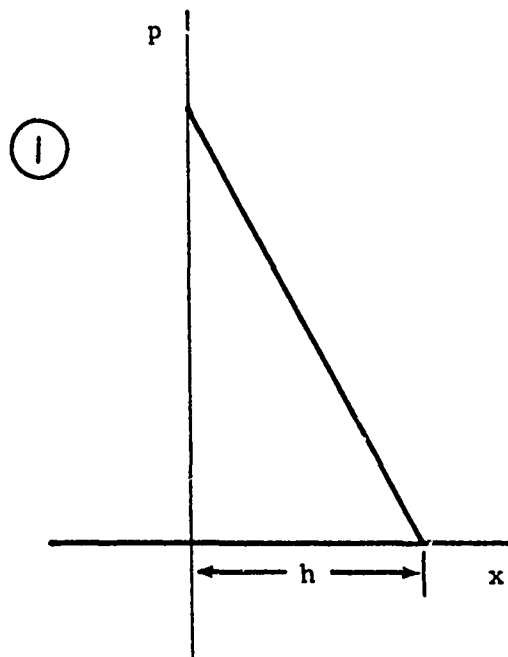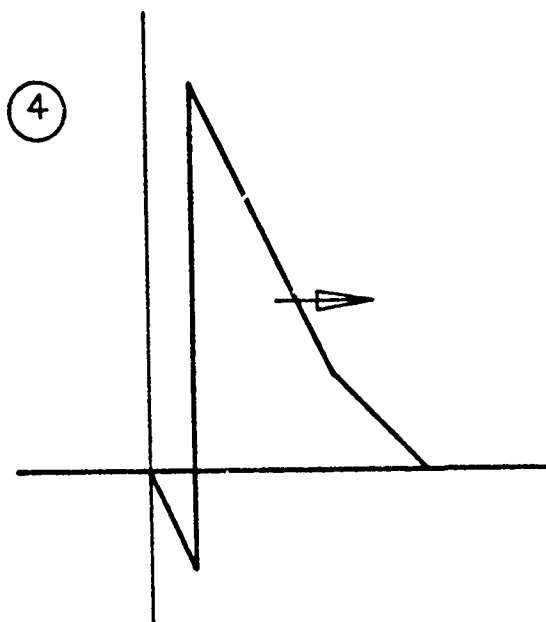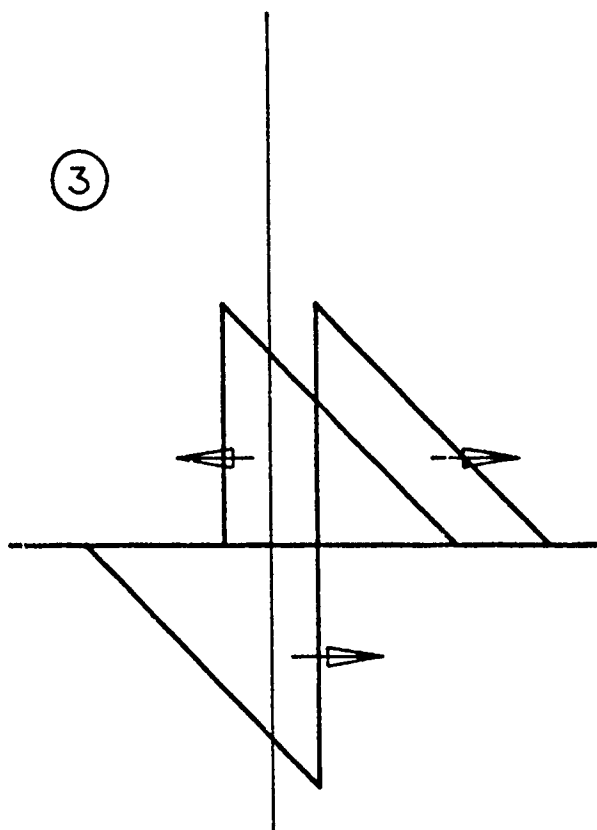
the part traveling left in shape and sign (sketch 3), that will at all times cancel that compressive pulse. The result of these three waves at the time Δt is shown in sketch 4.

After the pulses all clear the free surface, the result is a classical "N-shaped" wave as shown in sketch 5. Therefore, in this simplistic analysis, we can see that the net effect of an initial triangular energy deposition is a wave with a triangular compressive front followed by a triangular tensile tail of equal magnitude.
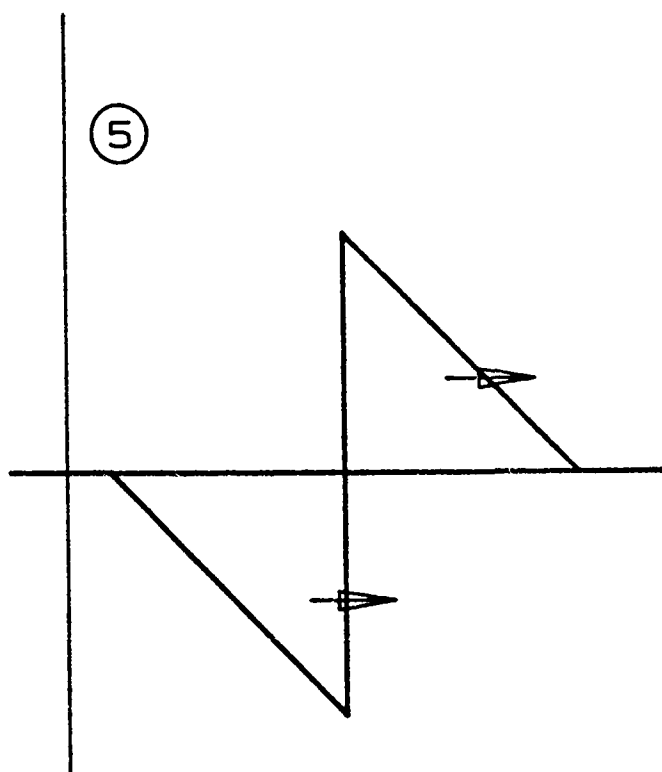
This analysis assumes instantaneous energy deposition. A slightly modified picture occurs when the deposition time t_o is not small compared to the pulse depth h divided by the wave speed c. In that case, for the same total energy and deposition depth, the final wave after deposition time will have a reduced peak and will have a total spatial width of $h + ct_o$. However, there will still be a following tensile tail of the same magnitude as the compressive front.

Real materials are not linear elastic, particularly at the high temperature and pressure states encountered during the energy deposition phase. The most important feature of nonelastic actual behavior will be a finite tensile strength, due either to the inherent strength of the solid, or due to the reduced strength of a vaporized or partially vaporized state.

Assume, for example, that the energy deposition magnitude is such that the peak compressive stress in the above sketches is 5 kilobars, and that the tensile spall strength is 1 kilobar. Then, at some time between the first growth of the tensile tail at the free surface and the time when the N-shaped wave would have left the free surface, the tensile stress at some distance in from the free surface will reach 1 kilobar, and tensile spall will occur. Indeed, with the values stated in this simple example, that initial spall thickness will be exactly one-fifth of the deposition depth h. That reduces the stress at the spall plane back to zero, and a tensile pulse will again begin to grow, resulting in a second spall of equal thickness. In the final analysis, the resulting wave propagating into the structure will have a tensile tail, but limited in magnitude to the tensile spall strength. In the example here, that tail would be limited to 1 kilobar.

The final stress wave profile will, of course, depend on the exact nature of the energy deposition. In a one-dimensional thermoelastic analysis neglecting vaporization and tensile strength, Paramasivam and Reismann (1986) (Reference 7) find a similar compressive/tensile wave resulting from a Gaussian deposition in space and time.

1.4 Assumptions

A complete analysis of this complicated thermomechanical problem is beyond the scope of this Phase I work, but there are a number of assumptions that may be made for the problem to become tractable for analysis. First, we tacitly assume that the energy flux is large enough to vaporize the first few plies but is not sufficiently strong to vaporize to a significant depth in the

plate. If we assume that the delamination does not reside too close to the upper surface, then the effects of the delamination will not be strongly coupled to the shock wave initiation. Hence, the interaction of the stress wave with the delamination may be treated separately from the physics of its initial generation. Furthermore, if we wish to analyze the stresses at the delamination in a planar setting, we are forced to make some assumptions regarding the areal extent of the energy deposition and the geometry of the delamination. We may assume either that the energy is uniformly distributed over an area much larger than the characteristic width of the delamination, or that the energy is deposited uniformly over a thin but very elongated region. The first assumption seems more realistic, but the second allows us to study effects related to the position of the energy deposition with respect to the delamination. The delamination itself must be regarded as having some large extension down the plate. In other words, the delamination is a long cavity with small width and even smaller thickness. With these assumptions, the deformation is uniform along the long axis of the delamination (and the energy deposition area), and the plate exists in a state of plane strain (Figure 3).

The assumption of a large uniform energy deposition further reduces the dynamics of the stress wave propagation to a one-dimensional problem, since the effects of the crack do not interact. Also, since the uniaxial stress-strain relation is independent of the ply orientation, the stress wave propagates as in a homogeneous material. It is only after the stress wave interacts with the delamination that the orthotropic, nonhomogeneous properties become apparent. Accordingly, if we assume that the initial stress wave is entirely compressive, and the closed delamination cannot slip (infinite friction), then the compressive wave will pass through unchanged.

With these assumptions, the problem may be approached with the two existing codes, FEAPICC, a two-dimensional, finite element code for propagating cracks between differing anisotropic materials, and WONDY, a one-dimensional, finite difference code modeling the thermomechanics of the energy deposition. Before moving on to a discussion of the simulations using these codes, the next section presents more details of the theoretical model.

9
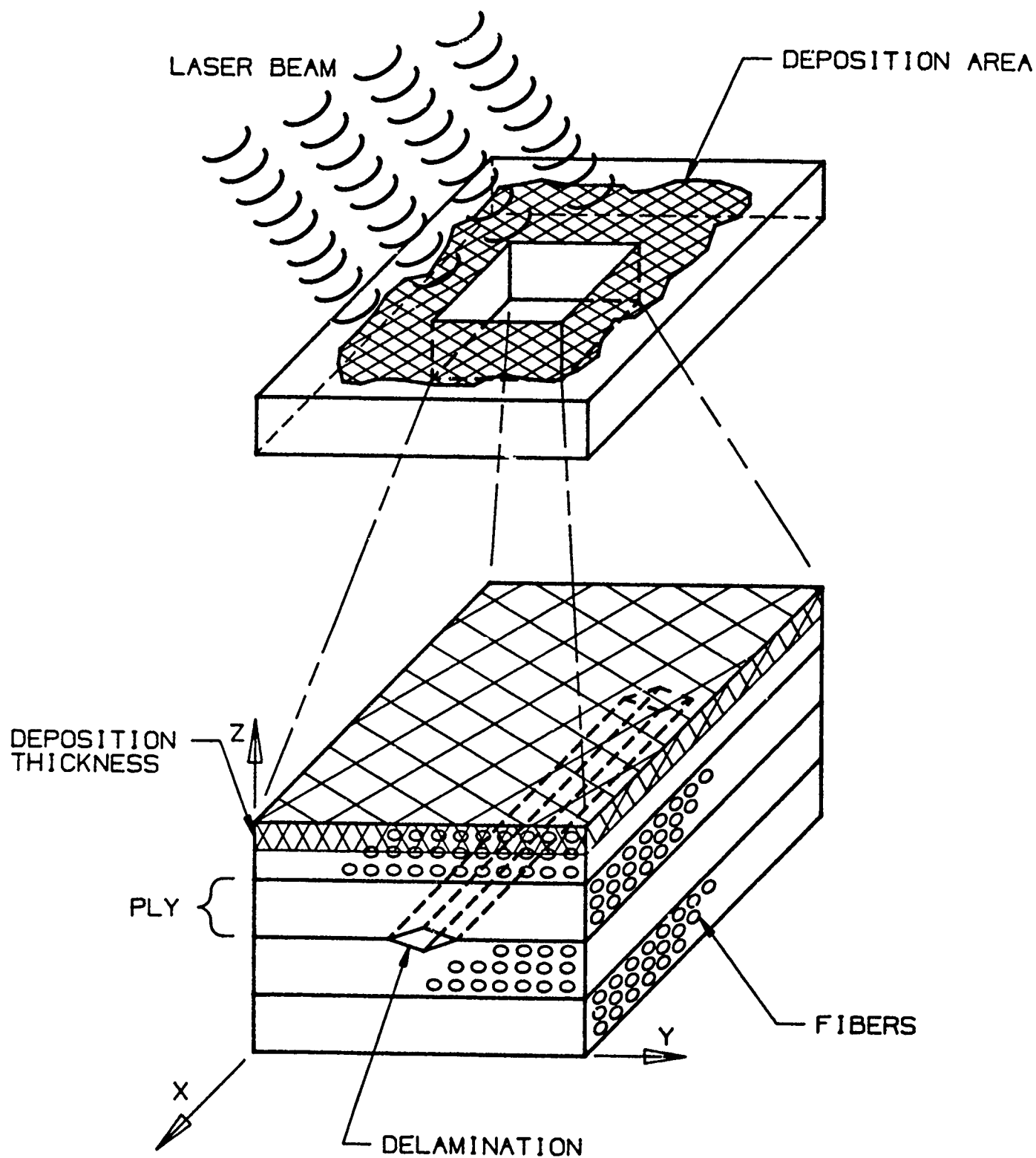
Figure 3.   Laser Energy Deposition on a Composite Plate

2. THEORETICAL DEVELOPMENTS

2.1 Continuum Mechanics Overview

We present here a brief description of the continuum model with emphasis on particular aspects that relate to the deposition of energy in composite laminates.

The motions are governed by the general equations of continuum mechanics, as are used in all studies of fluid, solid and structural mechanics. The computer codes used in this and other studies transcribe those equations into an approximate form suitable for solution on a computer.

The equations are recorded here in Lagrangian form. The position of a material point in a reference Lagrangian coordinate system is denoted by $\underset{\sim}{x}^o$. The spatial position $\underset{\sim}{x}$ is then a function of $\underset{\sim}{x}^o$ and time t:

$$\underset{\sim}{x} = \underset{\sim}{x} \, (\underset{\sim}{x}^o, t) \quad . \tag{1}$$

A variety of kinematic definitions include those for

$$\begin{array}{lll}
\text{Velocity:} & \underset{\sim}{v} = \dot{\underset{\sim}{x}} & \\[2mm]
\text{Acceleration:} & \underset{\sim}{a} = \dot{\underset{\sim}{v}} & \\[2mm]
\text{Deformation gradient tensor:} & \underset{\sim}{F} = \underset{\sim}{\nabla}^o \underset{\sim}{x} & (2) \\[2mm]
\text{Velocity gradient tensor:} & \underset{\sim}{L} = \dot{\underset{\sim}{F}} \, \underset{\sim}{F}^{-1} & \\[2mm]
\text{Stretching tensor:} & 2\underset{\sim}{D} = \underset{\sim}{L} + \underset{\sim}{L}^T &
\end{array}$$

Here the superposed dot denotes the material time derivative and $\underset{\sim}{\nabla}^o$ is the del operator with respect to $\underset{\sim}{x}^o$. The stress tensor is denoted by $\underset{\sim}{\sigma}$, which, to be precise, is the first Piola-Kirchhoff tensor related to the more standard Cauchy stress tensor $\underset{\sim}{T}$ by the relation

$$\underset{\sim}{\sigma} = J \, \underset{\sim}{T} \, (\underset{\sim}{F}^{-1})^T \tag{3}$$

with

$$J = \det \underset{\sim}{F} \quad . \tag{4}$$

The pressure p is given by

$$p = -1/3 \, \text{tr} \, \underset{\sim}{\sigma} \quad . \tag{5}$$

Using the symbol ρ to denote the mass density and ρ_o the density in the

reference configuration, the balance of mass can be written as

$$\dot{\rho} + \rho \underset{\sim}{\nabla} \cdot \underset{\sim}{v} = 0 \quad , \tag{6}$$

the balance of linear momentum as

$$\underset{\sim}{\nabla}^{o} \cdot \underset{\sim}{\sigma} + \rho_o \cdot \underset{\sim}{b} = \rho_o \cdot \underset{\sim}{a} \quad , \tag{7}$$

and, finally, the balance of energy as

$$\rho \dot{e} = tr(\underset{\sim}{T}\underset{\sim}{D}) - \underset{\sim}{\nabla} \cdot \underset{\sim}{q} + \rho r \quad , \tag{8}$$

where $\underset{\sim}{b}$ is the body force, $\underset{\sim}{q}$ is the heat flux vector and r is the deposited energy per unit mass.

These equations are supplemented by the constitutive equations describing the material. There is a relation between the internal energy e, the density ρ and the pressure p, which we write as

$$p = p(e, \rho) \tag{9}$$

While this single equation of state form is sufficient to describe completely the thermodynamics, it is more common to also include descriptions for the temperature T and entropy η:

$$T = T(e, \rho)$$
$$\eta = \eta(e, \rho) \tag{10}$$

Then these three thermodynamic equations can be solved to use any two thermodynamic variables as independent. The discussions of the previous section used T and ρ; the corresponding forms are given by

$$p = p(\rho, T)$$
$$e = e(\rho, T) \tag{11}$$
$$\eta = \eta(\rho, T)$$

and constant pressure or constant entropy states lie along some curve in $\rho - T$ space as described above. Phase boundaries become curves in this $\rho - T$ space.

To complete the description, a relation for the shear stress components is needed. This usually takes the form of equations for the stress deviator tensor:

$$\underset{\sim}{\sigma}_D = \underset{\sim}{\sigma} - p \underset{\sim}{\delta} \quad . \tag{12}$$

Relating the rate of change of $\underset{\sim}{\sigma}_D$ to the stretching tensor $\underset{\sim}{D}$ via a shear modulus G is usual. The shear modulus G can depend on the thermodynamic state,

i.e., the temperature and density. Plasticity relations are used to limit the values of the stress deviators when plastic flow occurs; the yield strength Y is also dependent on the thermodynamic state. Polymeric materials of composite structures may require more general and time-dependent models. Again, little is presently known about suitable models. The most that appear to be available are quasi-static dependences of strength and stiffness versus temperature, and only to the few hundred degrees for which composite materials maintain their primary structural integrity. Finally, fracture criteria are needed to describe spall (tensile failures) and, in the case of composite structures, ply delaminations.

It is clear that there is an imposing amount of information that goes into the final solution of these problems. Fortunately, there are well developed and tested finite difference codes, such as the one-dimensional code WONDY and the two-dimensional code CSQ that have been used in the present program. Provisions for a number of different material model types are available, as well as both analytical and tabular descriptions of the thermodynamics, including complete three-phase boundary descriptions and transitions. At the present, for normal wave-propagation studies, it must be said that the models are better developed than warranted; however, the experimental data to provide inputs to these models (or even to simply discover what type of a model is appropriate) are lacking. Furthermore, even for generic input models, the effects of composite laminations or delaminations on the wave propagation mechanics has not been considered. It is, of course, that issue that is the primary focus of the present study.

2.2 Singular Finite Element Formulation

In the present study, singular finite elements are used near the tip of a delamination crack to account for stress singularity at the crack tip. These elements incorporate stress and displacement fields from the closed-form solutions and therefore are extremely accurate and efficient. The singular elements are then combined with the regular isoparametric elements in the surrounding region so that the standard finite element procedures can be used to obtain displacement at each node.

The development of singular elements is based on a hybrid functional derived in Tong et al. (1973) (Reference 10). This hybrid functional was used by Lin and Mar (1976) (Reference 5) for the study of bi-material crack problems and recently by Aminpour and Holsapple (Aminpour, 1986) (Reference 1) for the

13

dynamic analysis of cracks between two anisotropic materials. For a two-dimensional continuum divided into m elements, the hybrid functional can be defined as

$$\Pi = \sum \Pi_m \tag{13}$$

where

$$\Pi_m = \int_{t_0}^{t_1} \left\{ \int_{V_m} \left[\frac{1}{2} \underset{\sim}{\varepsilon} \cdot (\underset{\sim}{\sigma} + \underset{\sim}{\sigma}^0) - \rho \underset{\sim}{u} \cdot \underset{\sim}{b} + \frac{1}{2} \rho \underset{\sim}{\dot{u}} \cdot \underset{\sim}{\dot{u}} \right] dV \right.$$
$$\left. + \int_{S_{in}} (\underset{\sim}{u} - \underset{\sim}{v}) \cdot \underset{\sim}{\tau} \, ds - \int_{S_0} \underset{\sim}{u} \cdot \overline{\underset{\sim}{\tau}} \, ds \right\} dt \; . \tag{14}$$

In the above, $\underset{\sim}{\sigma}$, $\underset{\sim}{\varepsilon}$, $\underset{\sim}{\sigma}^0$, and $\underset{\sim}{u}$ are the stress, strain, thermal stress and displacement, respectively. Other variables are the body force $\underset{\sim}{b}$, the density ρ and the tractions $\underset{\sim}{\tau}$ and $\overline{\underset{\sim}{\tau}}$ on the boundaries. The displacement $\underset{\sim}{v}$ along the interelement boundary S_{in} is assumed independently of the interior displacement $\underset{\sim}{u}$. The constraint integral over S_{in} is added to enforce the continuity of the displacements between the singular element and a regular element that uses different interpolation functions for the displacement components.

Making use of the stress, strain, and displacement fields obtained from the closed-form solution of a semi-infinite crack, we can assume

$$\underset{\sim}{u} = \underset{\sim}{U} \beta$$
$$\underset{\sim}{\sigma} = \underset{\sim}{A} \underset{\sim}{E} \beta + \underset{\sim}{\sigma}^0 \tag{15}$$
$$\underset{\sim}{\tau} = \underset{\sim}{R} \beta$$

where the β's are unknown constants to be determined from the finite element solution of the overall problem.

If the field variables in Equation (15) are used, then all elasticity equations are satisfied exactly at any time t, and the volume integral in the hybrid functional can be reduced to a boundary integral. The Euler equation for the variational functional is simply

$$\underset{\sim}{u} = \underset{\sim}{v} \qquad \text{on } S_{in}$$

and $$\tag{16}$$

$$\overline{\underset{\sim}{\tau}} = \underset{\sim}{n} \cdot \underset{\sim}{\sigma} \qquad \text{on } S_0$$

where $\underset{\sim}{n}$ is the normal vector.

The interelement boundary displacement $\underset{\sim}{u}$ can be assumed in the following form:

$$\underset{\sim}{u} = \underset{\sim}{L} \, q \tag{17}$$

14

in which q is the nodal displacement vector, and L is chosen such that u is comp.at. ·le with the surrounding regular elements. For example, L may be chosen to vary linearly between two nodes along the interelement boundary if constant strain elements are used in the surrounding.

Substituting the assumed quantities from Equations (15) and (17) into the hybrid functional and taking the variation of the functional with respect to β, we obtain (Aminpour, 1986) (Reference 1)

$$\beta = B \, q \quad \text{with} \quad B = P^{-1} G \tag{18}$$

and

$$\pi_m = \int_{t_o}^{t_1} \left(\frac{1}{2} q^T K q - \frac{1}{2} \dot{q}^T M \dot{q} - \dot{q}^T V q - q^T F \right) dt \tag{19}$$

where

$$K = B^T H B - B^T M_1 B - \dot{B}^T M_2 \dot{B} - 2 B^T M_3 \dot{B}$$

$$M = B^T M_2 B$$

$$V = B^T M_2 \dot{B} + B^T M_3 B \tag{20}$$

$$F = B^T F_s \quad .$$

The remaining matrices are defined as follows:

$$H = \int_{V_m} E^T A E \, dv$$

$$F_s = \int_{V_m} (U^T \rho b - E \sigma^o) \, dv$$

$$M_1 = \int_{V_m} \dot{U}^T \rho \dot{U} \, dv$$

$$M_2 = \int_{V_m} U^T \rho U \, dv \tag{21}$$

$$M_3 = \int_{V_m} \dot{U}^T \rho U \, dv$$

$$G = \int_{S_{in}} R^T L \, ds$$

$$P = \int_{S_{in}} R^T U \, ds$$

15

in which the dots denote the time derivatives and $\underset{\sim}{A}$ is the stress-strain relation matrix. The matrix $\underset{\sim}{E}$ is defined as

$$\underset{\sim}{E} = \begin{bmatrix} \frac{\partial}{\partial x} & 0 \\ 0 & \frac{\partial}{\partial y} \\ \frac{\partial}{\partial y} & \frac{\partial}{\partial x} \end{bmatrix} \underset{\sim}{U} \ . \tag{22}$$

In Equation (19), $\underset{\sim}{K}$ is the element stiffness matrix, $\underset{\sim}{M}$ is the mass matrix, $\underset{\sim}{V}$ is the damping matrix, and $\underset{\sim}{F}$ is the element force vector. These quantities can be assembled with regular elements using standard finite element procedures. The summation of π_m in Equation (19) over the entire domain and the use of variational theorems will yield the following governing differential equation for elasto-dynamic problems:

$$\underset{\sim}{M}\ddot{q} + \underset{\sim}{V}\dot{q} + \underset{\sim}{K}q = \underset{\sim}{F} \tag{23}$$

where $\underset{\sim}{M}$, $\underset{\sim}{V}$, $\underset{\sim}{K}$, and $\underset{\sim}{F}$ are assembled quantities. Although there is no damping considered in this problem, the matrix $\underset{\sim}{V}$, called the "pseudo-damping" matrix, is present. Also, for a propagating crack, the matrix $\underset{\sim}{M}$ is symmetric, while the matrices $\underset{\sim}{K}$ and $\underset{\sim}{V}$ are not, as can be seen from Equations (20) and (21). For a stationary crack, the matrix V vanishes and the matrix K becomes symmetric. The existence of the pseudo-damping matrix $\underset{\sim}{V}$ and the nonsymmetry of the $\underset{\sim}{K}$ matrix occur only in the formulation of singular elements. These complexities arise because the eigenfunctions for the singular element were derived with respect to a moving local coordinate system at the crack tip; therefore, the matrices $\underset{\sim}{M}$, $\underset{\sim}{V}$, and $\underset{\sim}{K}$ are functions of time.

The derivations of element stiffness and mass matrices for the surrounding regular elements can be found elsewhere, for example, in Aminpour (1986) (Reference 1).

2.3 Strain Energy Release Rate

The strain energy release rate is defined as the energy released per unit of new crack surface generated by a propagating crack. For a general two-crack problem, the strain energy release rate can be expressed by the following crack closure integral (Lawrence and Masur, 1971) (Reference 3):

$$G_T = \lim_{\delta \to 0} \frac{1}{\delta} \int_0^\delta \left\{ \frac{1}{2} \ \sigma_z(x,0)[w(x-\delta,0)] + \tau_{xz}(x,0)[u(x-\delta,0)] \right\} dx \tag{24}$$

where the first term in the integral can be defined as G_1 (mode 1) and the second term as G_2 (mode 2). The stresses are evaluated at a distance x ahead of the crack tip and the corresponding displacements are calculated at a distance $\delta - x$ behind the tip of a crack.

In the present study, the stress and displacement are obtained from an eigen-function expansion method with each term accurate to a constant β_i. The $\underset{\sim}{\beta}$ matrix is then determined by matching the local crack-tip solution (singular elements) with far-field solutions (regular elements). Once $\underset{\sim}{\beta}$'s are found, the stresses and displacements are known, and Equation (24) can be integrated numerically. Note that since the stress or strain is oscillating near the tip of an interface crack between two different materials, the G_1 and G_2 results as obtained from Equation (24) generally depend upon the δ values chosen (Froula et al., 1980) (Reference 2). Therefore, the usefulness of separate G_1, G_2 values for bi-material crack problems remains to be studied. However, the total strain energy release rate G_T has been shown to be independent of δ (Walker and Lin, 1987) (Reference 11).

2.4 Plane Strain

Consider a lamina whose fibers lie in the XY plane as shown in Figure 3. Consider this ply to be a monoclinic material with a stress/strain relation of the form

$$\begin{Bmatrix} \epsilon_x \\ \epsilon_y \\ \epsilon_z \\ \gamma_{yz} \\ \gamma_{xz} \\ \gamma_{xy} \end{Bmatrix} = \begin{bmatrix} S_{11} & S_{12} & S_{13} & 0 & 0 & S_{16} \\ S_{12} & S_{22} & S_{23} & 0 & 0 & S_{26} \\ S_{13} & S_{23} & S_{33} & 0 & 0 & S_{36} \\ 0 & 0 & 0 & S_{44} & S_{45} & 0 \\ 0 & 0 & 0 & S_{45} & S_{55} & 0 \\ S_{16} & S_{26} & S_{36} & 0 & 0 & S_{66} \end{bmatrix} \begin{Bmatrix} \sigma_x \\ \sigma_y \\ \sigma_z \\ \tau_{yz} \\ \tau_{xz} \\ \tau_{xy} \end{Bmatrix} + \begin{Bmatrix} \alpha_1 \\ \alpha_2 \\ \alpha_3 \\ 0 \\ 0 \\ \alpha_6 \end{Bmatrix} T \qquad (25)$$

where S_{ij} is the compliance matrix and α_i is the coefficient of thermal expansion. Here, we use the contracted notation for stress and strain and T is the temperature above the reference.

Assume that the deformations are independent of the X direction so that

$$\epsilon_x = \gamma_{xz} = \gamma_{xy} = 0 \qquad (26)$$

for which we may solve for stresses acting on the X face.

17

$$\sigma_x = \frac{1}{d}\ (S_{16}S_{26} - S_{66}S_{12})\sigma_y + (S_{16}S_{36} - S_{66}S_{13})\sigma_z + (S_{16}\alpha_6 - S_{66}\alpha_1)T$$

$$\tau_{xy} = \frac{1}{d}\ (S_{12}S_{16} - S_{11}S_{26})\sigma_y + (S_{16}S_{13} - S_{36}S_{11})\sigma_z + (S_{16}\alpha_1 - S_{11}\alpha_6)T \qquad (27)$$

$$\tau_{xz} = -\frac{S_{45}}{S_{55}}\ \tau_{yz}$$

with

$$d = S_{11}S_{66} - S_{16}^2\ . \qquad (28)$$

Substituting these expressions back into the three-dimensional stress/strain relations and adopting the two-dimensional stress/strain definition as

$$\left\{\begin{array}{c} \epsilon_y \\ \epsilon_z \\ \gamma_{yz} \end{array}\right\} = \left[\begin{array}{ccc} b_{11} & b_{12} & 0 \\ b_{12} & b_{22} & 0 \\ 0 & 0 & b_{33} \end{array}\right] \left\{\begin{array}{c} \sigma_y \\ \sigma_z \\ \tau_{yz} \end{array}\right\} + \left\{\begin{array}{c} \alpha_y \\ \alpha_z \\ 0 \end{array}\right\}T\ , \qquad (29)$$

then

$$b_{11} = S_{22} + (2\ S_{12}S_{16}S_{26} - S_{66}S_{12}^2 - S_{11}S_{26}^2)/d$$

$$b_{22} = S_{33} + (2\ S_{13}S_{16}S_{36} - S_{66}S_{13}^2 - S_{11}S_{36}^2)/d$$

$$b_{12} = S_{23} + (S_{16}S_{12}S_{36} + S_{16}S_{26}S_{13} - S_{66}S_{13}S_{12} - S_{11}S_{26}S_{36})/d$$

$$\qquad (30)$$

$$b_{33} = S_{44} - S_{45}^2/S_{55}$$

$$\alpha_y = \alpha_2 + \left(\frac{S_{26}S_{16} - S_{66}S_{12}}{d}\right)\alpha_1 + \left(\frac{S_{12}S_{16} - S_{26}S_{11}}{d}\right)\alpha_6$$

$$\alpha_z = \alpha_3 + \left(\frac{S_{36}S_{16} - S_{66}S_{13}}{d}\right)\alpha_1 + \left(\frac{S_{13}S_{16} - S_{36}S_{11}}{d}\right)\alpha_6$$

Note that under the plane strain assumption, the material behavior becomes orthotropic. This is as expected, since, depending on the orientation of the fibers, the YZ plane cuts the fibers in circles, ellipses, or straight lines, as seen in Figure 4.

18

$\theta=0°$

$\theta=45°$

$\theta=90°$
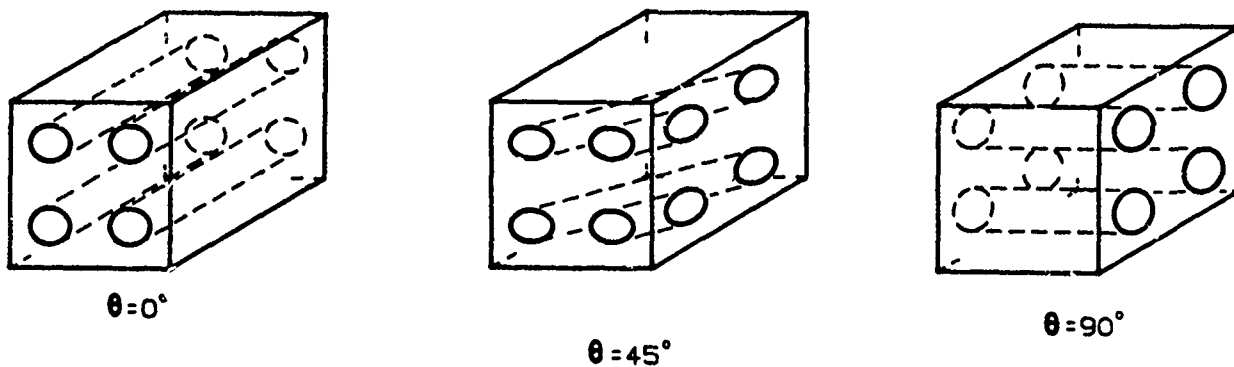
Figure 4. Plane Sections of a Laminate

The inverse relationship is given as

$$\left\{\begin{array}{c} \sigma_y \\ \sigma_z \\ \tau_{yz} \end{array}\right\} = \left[\begin{array}{ccc} a_{11} & a_{12} & 0 \\ a_{12} & a_{22} & 0 \\ 0 & 0 & a_{33} \end{array}\right] \left\{\begin{array}{c} \epsilon_y - \alpha_y T \\ \epsilon_z - \alpha_z T \\ \gamma_{yz} \end{array}\right\} \tag{31}$$

where

$$a_{11} = b_{22}/a \qquad a_{12} = -b_{12}/a$$

$$a_{22} = b_{11}/a \qquad a_{33} = 1/b_{33}$$

$$a = b_{11}b_{22} - b_{12}^2 . \tag{32}$$

19

3. FINITE ELEMENT VALIDATION TEST

In order to carry out this study, the FEAPICC code was transported from a CDC 60-bit computer to the Apollo 32-bit machine. This necessitated converting the code from single precision to double precision. However, since no double-precision complex arithmetic is available on the Apollo, most of the singular element computations were left in complex form with no apparant loss in precision. Conversion to double precision was especially important for dynamic problems and problems with many unknowns.

In addition to these conversion problems, new theoretical developments and applications and new I/O formats necessitated other modifications that required testing. This section documents tests performed to validate the accuracy of the code.

3.1 Singular Element Test

This section investigates the accuracy of the singular element when its dimensions become small compared to the size of the delamination. A typical ply thickness of a composite is on the order of 0.005 inch, while the delamination itself may be as large as 1 inch. Although nondestructive tests would rule out such a large delamination, it is conceivable that a delamination could grow to such lengths under normal operating conditions. To represent the stress variation properly, one or two elements would be required to lie within each ply. We find that the ratio of the crack length to the singular element size may be very large. A simple static analysis shows that the stresses grow by the square root of the ratio of the crack length to the distance to the crack tip. If the singular element occupies such a small region around the crack tip, this means that regular isoparametric elements next to the singular element must resolve large stress gradients.

O'Leary (1981) (Reference 6), in a one-dimensional error analysis and supporting numerical studies, shows that as the singular element becomes small, the error, in the energy norm, converges to zero. However, the rate of convergence suddenly slows after the singular is reduced below a certain size. The rate of convergence then becomes that which would be expected if no singular element was employed. The error in the stress intensity factor shows similar behavior except that no convergence is observed after the singular element is reduced below a certain size. In any case, the errors were significantly improved by the use of the singular element over computations that employed no

20

singular element, and no degradation of accuracy was observed as the singular element became small. This study leads us to be optimistic that the small singular element, in our more realistic two-dimensional cracks between different materials, would also be well behaved. To confirm this, we studied a model problem on two different meshes, one in which the singular element is the same size as the crack, and another for which the singular element is 20 times smaller. In addition, we have calculated the stresses using an entirely different program (FEAMOD) that employs an element with a singular transformation to capture the square root behavior (Stern, 1979) (Reference 9). The difference between this element and the singular element employed in FEAPICC is the form of the basis functions. Recall that the FEAPICC singular element basis is the set of the first 16 eigenfunctions forming the exact solution to the problem. For instance, the basis includes the sinusoidal log r behavior exhibited by cracks between different elastic materials.

The model problem, shown schematically in Figure 5, is that of a crack between two different isotropic materials with the upper material 100 times stiffer than the lower material. Solutions were computed with FEAPICC on the coarse grid shown in Figure 6 and on the fine grid in Figure 7. The coarse grid singular element is shown by the shaded region in Figure 6. The fine grid singular elements is a square one-tenth of the crack length on edge. The grid for the FEAMOD solution is shown in Figure 8 with the singular element made up of eight triangular elements covering the area inscribed by a circle of one crack length in diameter. The isoparametric elements in the FEAMOD solution are parabolic.

Table 1 shows the stress intensity factors for each of the three numerical solutions plus the exact solution of the problem (Rice and Sih, 1965) (Reference 8). The two FEAPICC solutions are more in agreement than the FEAMOD solution, which indicates one of two points. This difference may just be indicative that the stress

Table 1. Stress Intensity Model Comparison

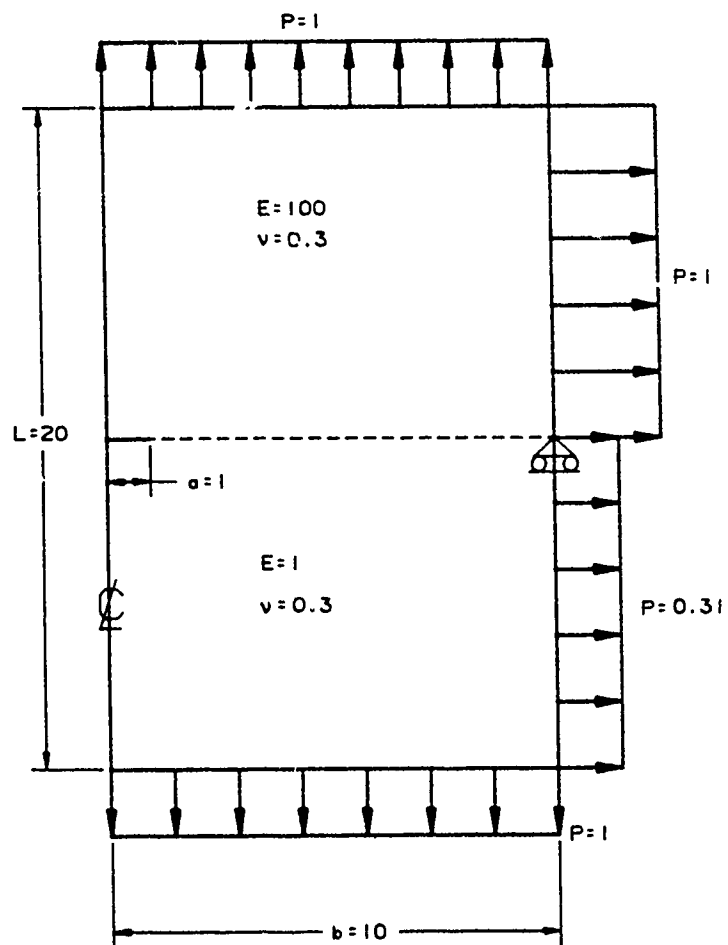| Model	K_1	K_2
FEAPICC (coarse)	1.777	−0.285
FEAPICC (fine)	1.809	−0.291
FEAMOD	1.542	−0.300
EXACT	1.793	−0.262

Figure 5. Crack Between Different Isotropic Materials
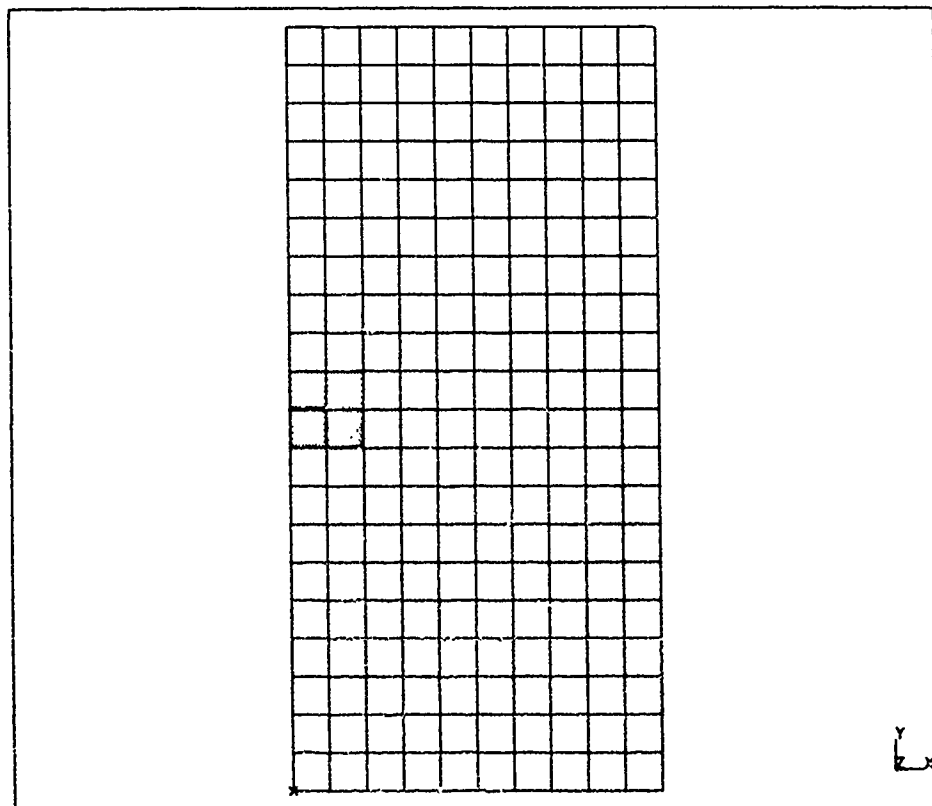

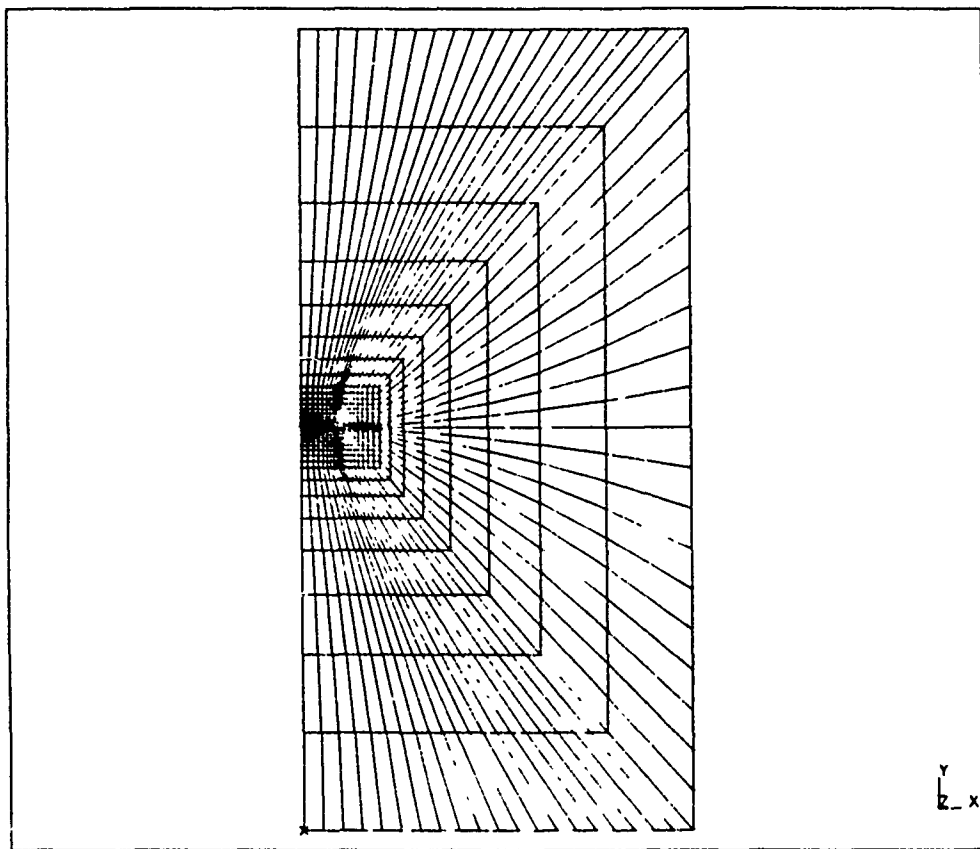Figure 6. Coarse FEAPICC Grid
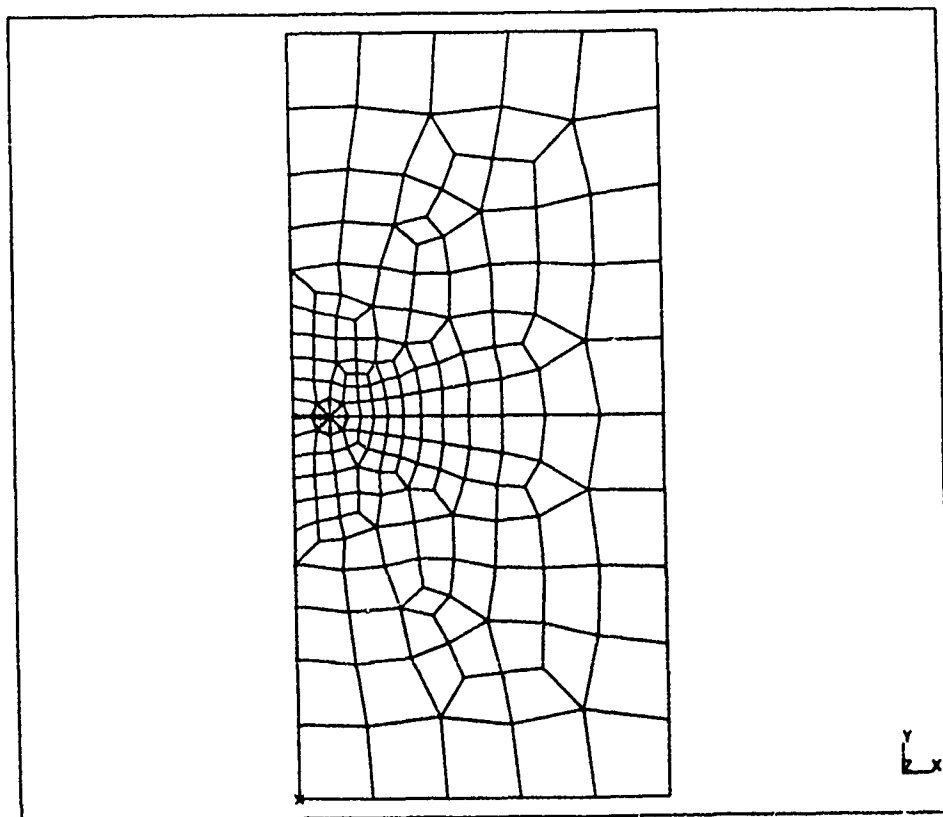
22

Figure 7.   Fine FEAPICC Grid

Figure 8.   FEAMOD Grid

23

intensity definitions are different for the FEAMOD and FEAPICC singular element, or it may show a real difference in the solutions. Comparing the Y normal stress contours in the vicinity of the crack on the exaggerated deformed geometry also shows some differences in the stress field suggesting that the FEAPICC singular element gives more well-behaved results. Figures 9, 10, and 11 show the stress contours for the FEAPICC coarse and fine grid solutions and the FEAMOD solution, respectively. To plot the results for the coarse FEAPICC and FEAMOD solutions, the stresses and displacements on the singular element have been interpolated to much finer, linear elements. The results of the fine grid singular element have not been interpolated to yet a finer grid, which explains the weaker contour gradients near the crack tip.

The close agreement between the coarse and fine grid solutions gives us some confidence that a large ratio of crack length to element length will not pose any problems. This may be especially true for shock wave problems in which the shock width may be much smaller than the delamination length. Hence, the stress concentration effects are localized near the crack tip, since, to the shock wave, most of the delamination looks like one uninterrupted free surface. Indeed, numerical experiments, to be described later, indicate such a localization.

3.2 Thermal Stress Validation

To test the implementation of the thermal stresses in the FEAPICC code, the singular finite element solution is compared to a simple analytical solution that has no singularity. The singular solution should be in close agreement except near the crack. In the problem shown in Figure 12, the temperature varies linearly across the plate in plane stress. With the loading as shown, the closed form solution for an isotropic, homogeneous plate is

$$
\begin{aligned}
u &= -\nu\sigma\, x/E + \alpha\, T_0 xy/L \\
v &= \sigma\, y/E + \alpha\, T_0(y^2 - x^2)/2L \quad .
\end{aligned}
\tag{33}
$$

The finite element solution has a small crack of length L/20 starting at $y = L/2$, $x = 0$. Except in the vicinity of this crack, the solution compares closely to the analytical solution. Table 2 compares the two solutions for various points on the plate. The displacement at the crack is an average of the top and bottom surfaces of the crack.
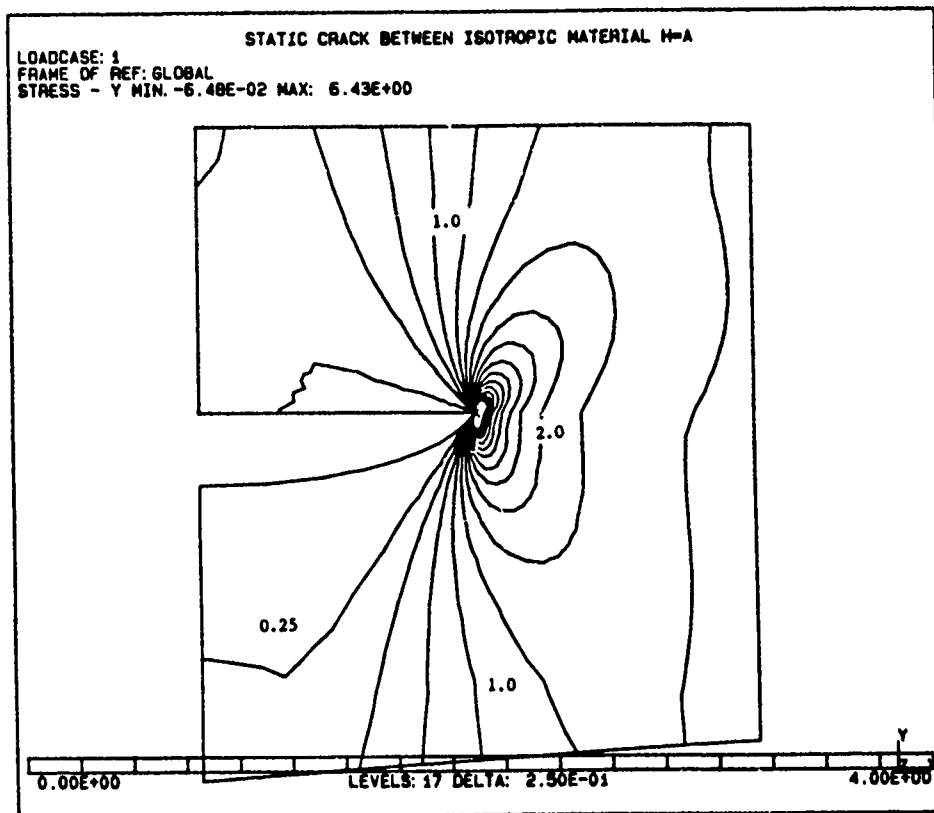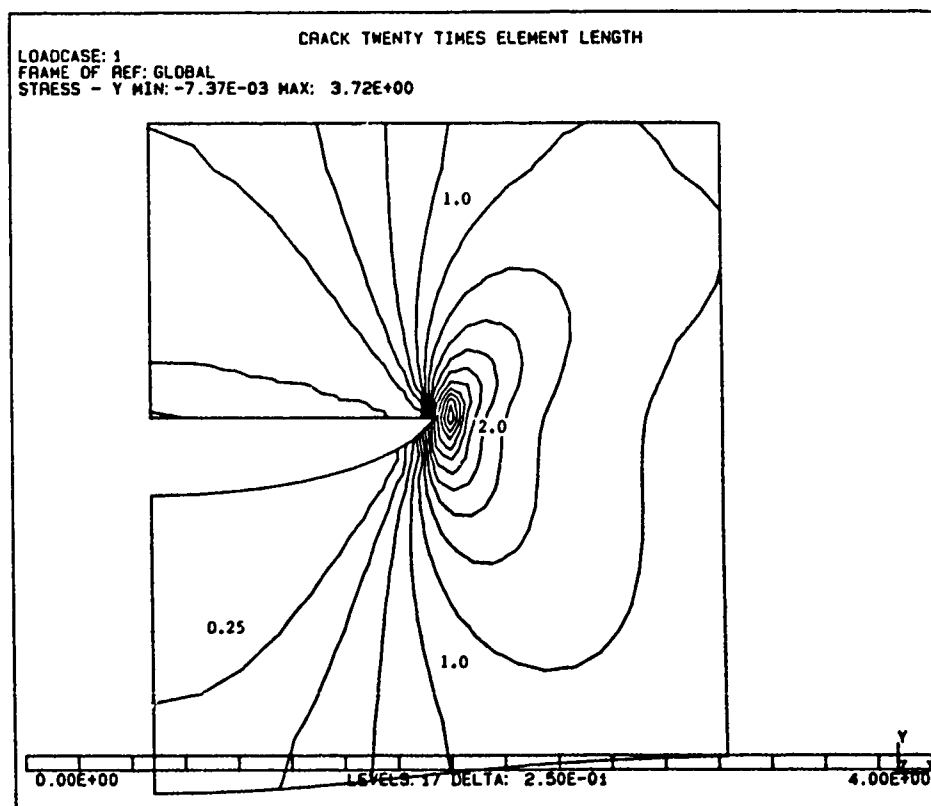
Figure 9. Normal Stress FEAPICC Coarse Grid

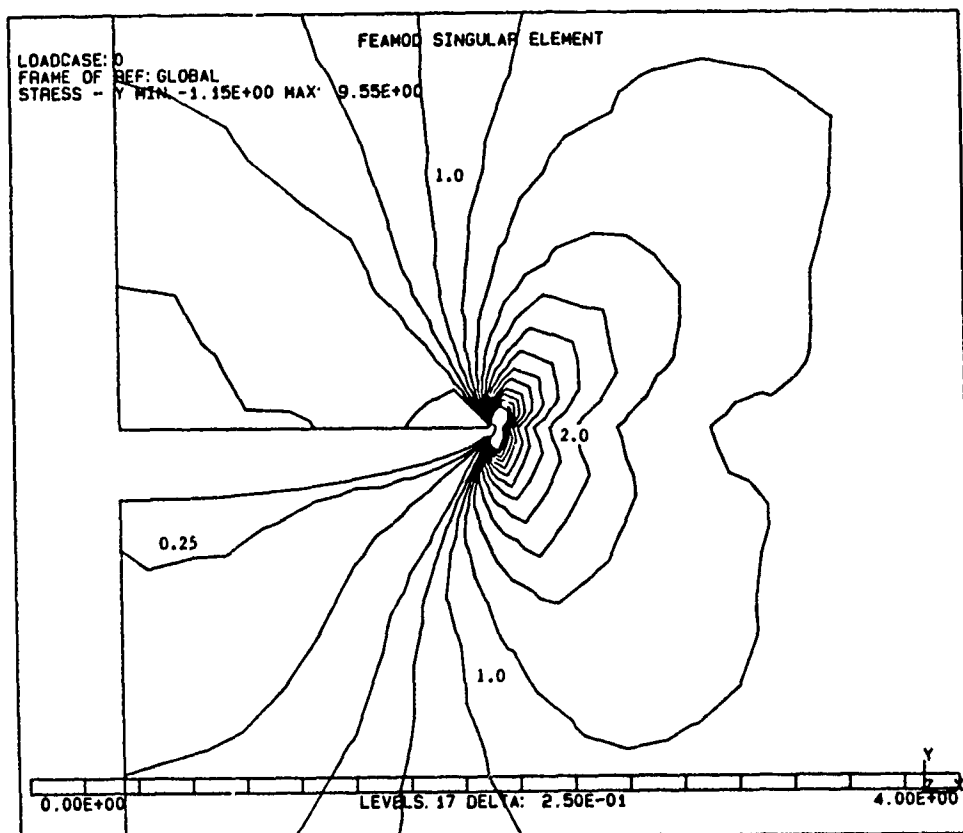Figure 10. Normal Stress FEAPICC Fine Grid

25

Figure 11. Normal Stress FEAMOD Solution
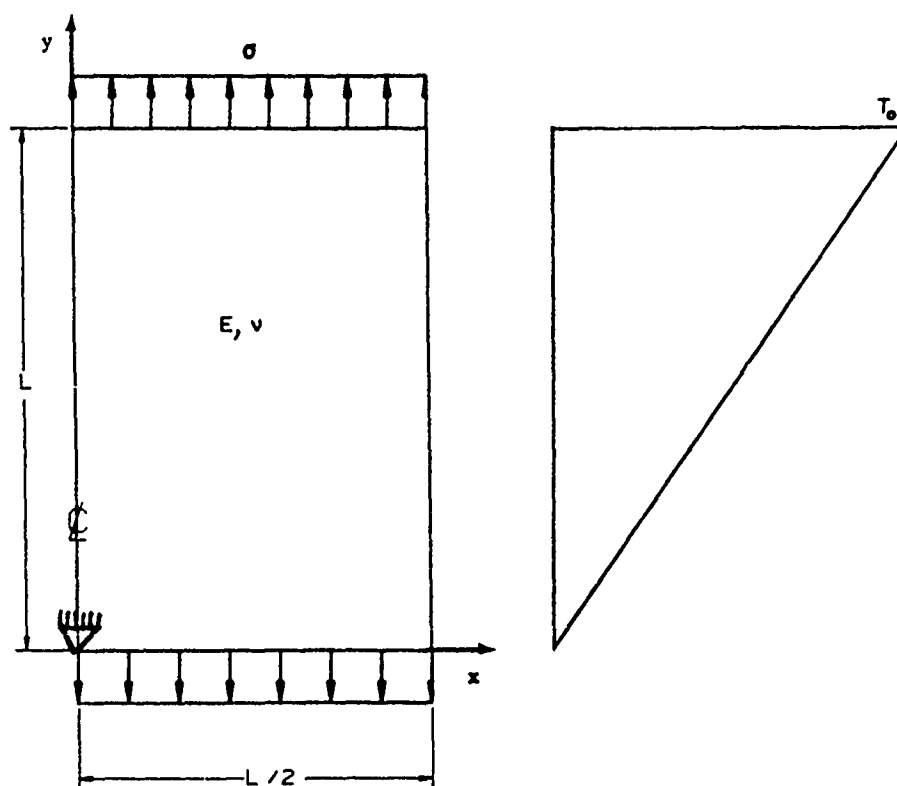
Figure 12. Thermal Stress Test Problem

Table 2. Static Thermoelastic Test Case Comparison
(L = 20, α = 1.0, E = 1.0, ν = 0.25, ΔT = 1.0)

x	y	u		v	
		EXACT	FEM	EXACT	FEM
0	0	0	0	0	0
5	0	-1.25	-1.17	-0.62	-0.50
10	0	-2.50	-2.41	-2.50	-2.19
0	5	0	0	5.62	5.57
5	5	0	-0.07	5.0	5.15
10	5	0	-0.10	3.12	3.43
0	10	0	0	12.5	12.89
5	10	1.25	0.94	11.87	11.81
10	10	2.5	2.26	10.0	10.21
0	15	0	0	20.62	21.09
5	15	2.5	2.42	20.0	20.26
10	15	5.0	4.89	18.12	18.23
0	20	0	0	30.0	30.41
5	20	3.75	3.83	29.37	29.66
10	20	7.5	7.58	27.5	27.61

3.3 Static Composite Plate Validation Test

In this section, we investigate the static response of a multi-ply plate with a centered delamination that has dimensions much larger than the ply thickness. The objective is to test the proper implementation of the planar stress/strain relations with a more realistic material model. The grid and loading for these tests is shown in Figure 13. The plate consists of eight plies with two elements within each ply. The material properties, typical of graphite-epoxy, are given in Table 3. Two composite plates are considered: a center symmetric plate (s) with fibers lying in the successive plies starting from the bottom at θ = 0°, 45°, 90°, -45°, -45°, 90°, 45°, and 0° and an unsymmetric plate (u) with successive plies at θ = 0°, 45°, 90°, -45°, 0°, 45°, 90°, -45°. The two different composites have been subjected to three different uniform temperature distributions:

(1) plate at reference temperature, ΔT = 0 (off);

(2) plate below reference temperature, ΔT = -0.1°F (cold); and

(3) plate above reference temperature, ΔT = 0.1°F (hot),

and two pressure loads:

(1) no mechanical load (off) and

(2) a load of 1 psi (on).

27
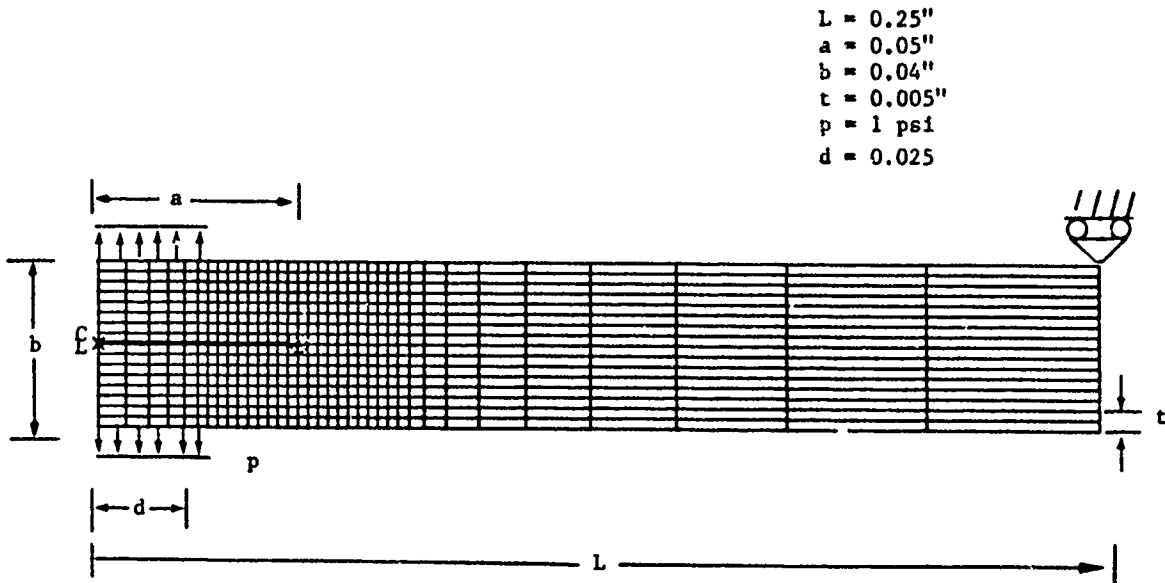
Figure 13. Composite Grid

L = 0.25"
a = 0.05"
b = 0.04"
t = 0.005"
p = 1 psi
d = 0.025

Table 3. Material Properties Along the Principal Coordinates
of the Fiber Direction

$E_1 = 1.8 \times 10^7$ psi	$E_2 = E_3 = 1.4 \times 10^6$ psi
$\nu_{12} = \nu_{13} = 0.34$	$\nu_{23} = 0.4 \qquad \rho = 0.055$ lb/in^3
$G_{12} = G_{13} = 0.95 \times 10^6$ psi	$G_{23} = 0.5 \times 10^6$ psi
$\alpha_1 = 2.0 \times 10^{-7}$ (°F)$^{-1}$	$\alpha_2 = \alpha_3 = 1.6 \times 10^{-5}$ (°F)$^{-1}$

The magnitudes of the thermal loads are chosen so that they are approximately the same magnitude as the pressure loads. Table 4 shows the stress intensity factors for each ply stacking, pressure, and thermal loading.

It is easy to show that the stress intensity factors behave as a linear function of the mechanical load and thermal load. Also, the strain energy release rate is a quadratic function of the mechanical load and the thermal load. The numerical results in Table 4 indicate that the strain energy release rate shows a strong coupling between the mechanical load and the thermal load. This implies that the strain energy resulting from a combined mechanical and thermal load is not simply the sum of the strain energies of each load independently.

28

Table 4. Static Composite Ply Stress Intensity Factors

ply stack	mech load	thermal loading	K_1 $\times 10^{-1}$ psi in	K_2 $\times 10^{-1}$ psi in	G_1 $\times 10^{-7}$ lb/in	G_2 $\times 10^{-7}$ lb/in	G $\times 10^{-7}$ lb/in
s	on	off	7.14	0	5.46	0	5.46
u	on	off	6.63	0.608	5.27	0.171	5.45
s	on	cold	8.88	-5.47	9.05	1.65	10.7
u	on	cold	8.64	-1.66	8.45	1.64	10.1
s	on	hot	5.40	5.47	2.76	1.65	4.41
u	on	hot	4.61	2.87	2.83	0.202	3.03
s	off	cold	1.74	-5.47	0.448	1.65	2.10
u	off	cold	2.02	-2.27	0.366	0.751	1.11

3.4 Dynamic Composite Plate Validation Test

Before moving to the actual simulation of the stress pulses generated by laser heating, we examine in this section the stress wave propagation generated by a pulsed tensile loading on the surface of the plate. We chose a pulse loading that is characteristic of that produced by pulsed laser after the back free surface reflection. The grid shown in Figure 13 and the symmetric stacking sequence and material properties described in Section 3.2 are used in this simulation. With these material properties we find a maximum longitudinal wave speed of 3.6×10^5 in/s along the fiber direction. The transverse longitudinal wave speed is about 1.0×10^5 in/s, while the shear wave speed ranges from 0.6×10^6 in/s in the 0° ply to 0.8×10^5 in/s in the 90° ply. Since the smallest grid dimension is 2.5×10^{-3} in, a step size of 5.0×10^{-9} s allows the fastest wave to traverse less than one element in one step.

In our simulations we noted severe oscillation problems with a square tensile loading pulse wave. These oscillations are characteristic of the element's inability to resolve the sharp front of the wave. To remove this effect, we selected a hat-shaped pulse loading in which the loading increases linearly with time until some maximum is reached and then falls linearly back to zero. The time to reach maximum loading is set to 2.0×10^{-7} s. This produces

29

a stress wave within the body that rises and falls within eight elements or four ply widths, and the oscillations are only modest. Ratios of half-wavelength to element size smaller than four show marked oscillations regardless of the step size using the Newmark method. The Wilson method with its inherent numerical damping proved to be only a slightly better option, since little damping was apparent for small time step sizes and too much damping or loss in accuracy was observed for the larger step sizes. These wave resolving restrictions have some important implications especially for sharp laser pulses in three-dimensional simulations, which we discuss further in Section 6.

In Figures 14 through 23, we show the stress contours at different times for the simulation of the symmetric plate. These contours are plotted on the exaggerated deformed geometry. Since the tensile load at a maximum of 1.0×10^6 psi is applied uniformly across the top surface, the stress wave is very uniform before it interacts with the delamination. In Figure 14, we see the normal transverse wave at a time just before its head reaches the delamination and before the end of the boundary loading pulse. Note that the delamination (marked by the line ending with the asterisk) is assumed closed initially. Although the delamination is initially in the center, the tensile deformation in the wave has stretched the top plies in this exaggerated plot. In Figure 15, the transverse normal stress is shown as the maximum stress passes in front of the crack. We see that the delamination has opened almost uniformly across its length. Also, we see the first signs of a compression wave reflecting off the free surface of the delamination. Five hundredths of a microsecond later (Figure 16) the compression wave is more fully developed, and still later (Figure 17) we see the interaction of the compression and tensile waves with the upper and lower surfaces. The stress intensity factors labeled on each plot show that these peak when both large compression and tensile stresses are near the crack tip. The shear wave propagates in a characteristic antisymmetric profile as shown in Figures 18 through 20. The time sequence of the longitudinal normal stress shown in Figures 21 through 23 indicates the dramatic effects of fiber stiffening. In the 90° plies the fibers are running parallel to the long axis. Since the waves travel over 3 times faster in 90° plies, we see that the contours seem to spurt out in these plies.

LOADCASE: 15 TIMESTEP: 15 TIME: 0.00000015
FRAME OF REF: GLOBAL
STRESS - Y MIN: -3.17E+03 MAX: 9.61E+04

$K_1 = -4.8 \times 10^1$

$K_2 = 3.0$

7.0

7.0

1.0

-9.00E+ LEVELS: 10 DELTA: 2.00E+04 9.00E+04
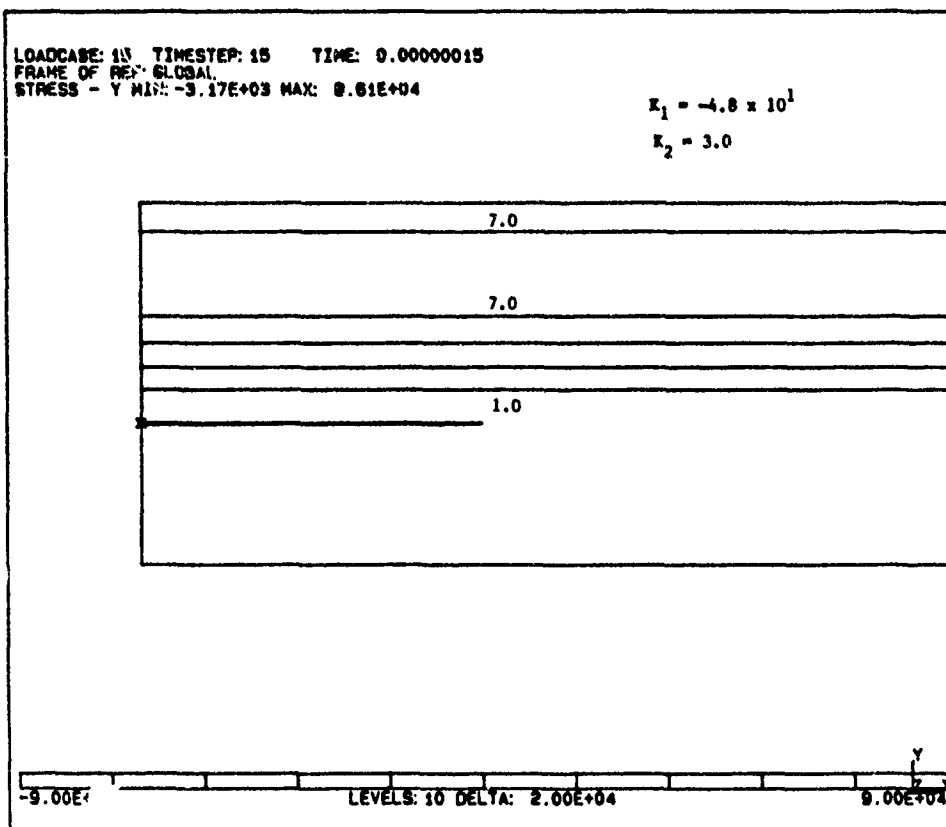
Figure 14. Normal Stress (t = 0.15 μs)

LOADCASE: 30 TIMESTEP: 30 TIME: 0.0000003
FRAME OF REF: GLOBAL
STRESS - Y MIN: -2.26E+04 MAX: 1.00E+05

$K_1 = 8.4 \times 10^3$

$K_2 = -3.1 \times 10^1$

-1.0   1.0

7.0

9.0

7.0

1.0

-9.00E+04 LEVELS: 10 DELTA: 2.00E+04 9.00E+04
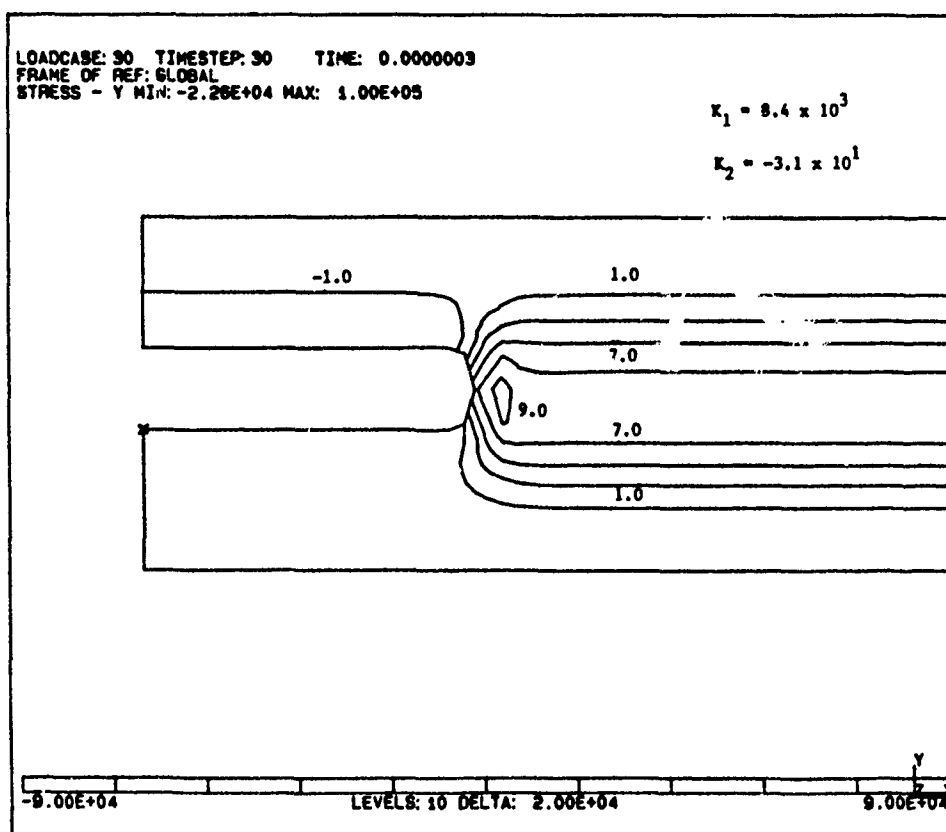
Figure 15. Normal Stress (t = 0.3 μs)

31

LOADCASE: 35   TIMESTEP: 35   TIME: 0.00000035
FRAME OF REF. GLOBAL
STRESS – Y MIN.-8.05E+04 MAX: 8.41E+04

$K_1 = 8.7 \times 10^3$

$K_2 = -2.2 \times 10^1$

-9.00E+04   LEVELS: 10 DELTA: 2.00E+04   9.00E+04
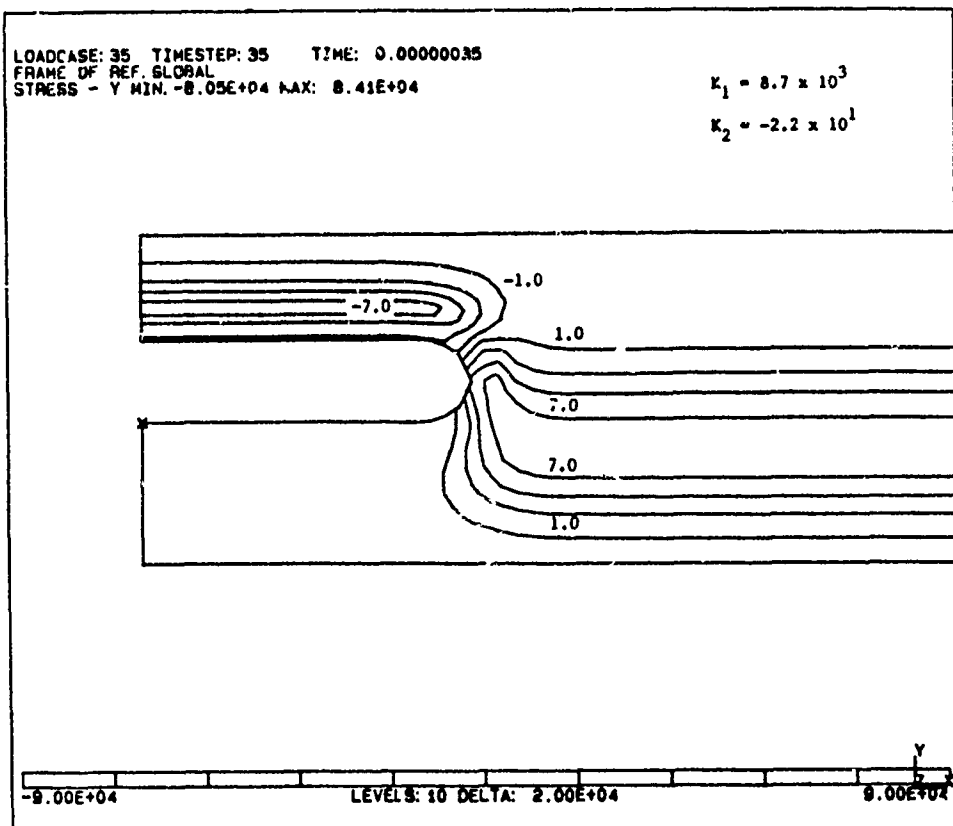
Figure 16.   Normal Stress (t = 0.35 μs)

LOADCASE: 40   TIMESTEP. 40   TIME: 0.0000004
FRAME OF REF: GLOBAL
STRESS – Y MIN:-8.89E+04 MAX: 8.98E+04

$K_1 = 6.6 \times 10^3$

$K_2 = 8.2$

-9.00E+04   LEVELS: 10 DELTA: 2.00E+04   9.00E+04
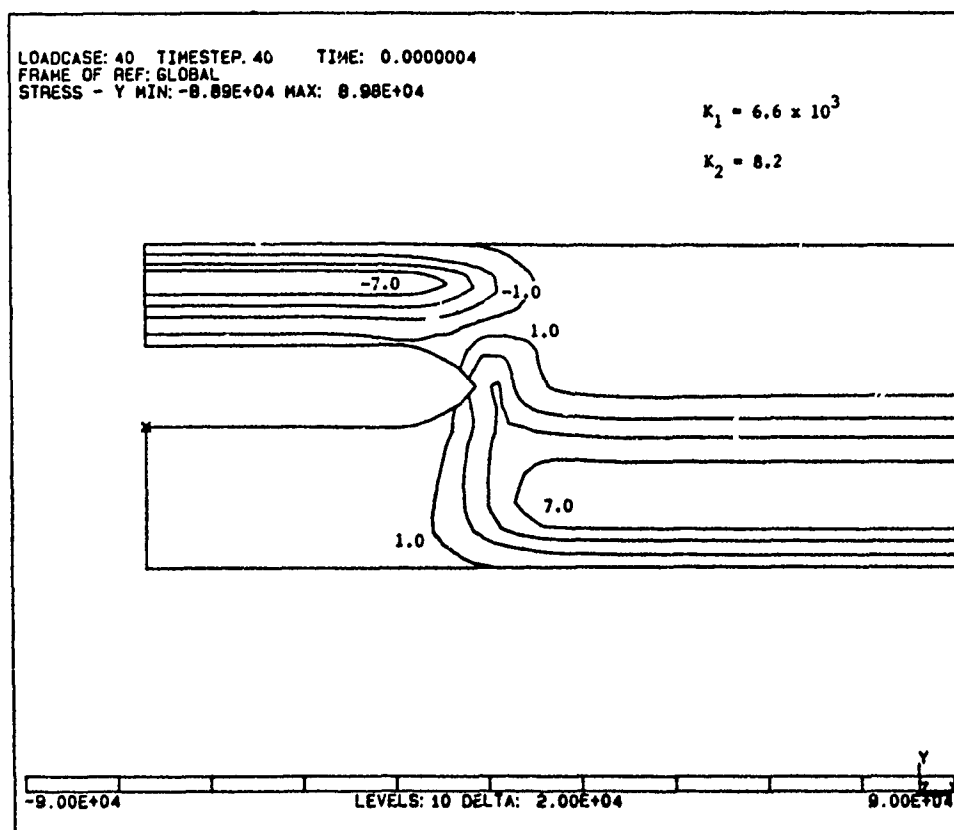
Figure 17.   Normal Stress (t = 0.4 μs)

32

LOADCASE: 30 TIMESTEP: 30 TIME: 0.00000C3
FRAME OF REF: GLOBAL
STRESS - XY MIN: -2.43E+04 MAX: 2.36E+04

-0.3
-2.1
2.1
0.3

-2.70E+04   LEVELS: 10 DELTA: 6.00E+03   2.70E+04
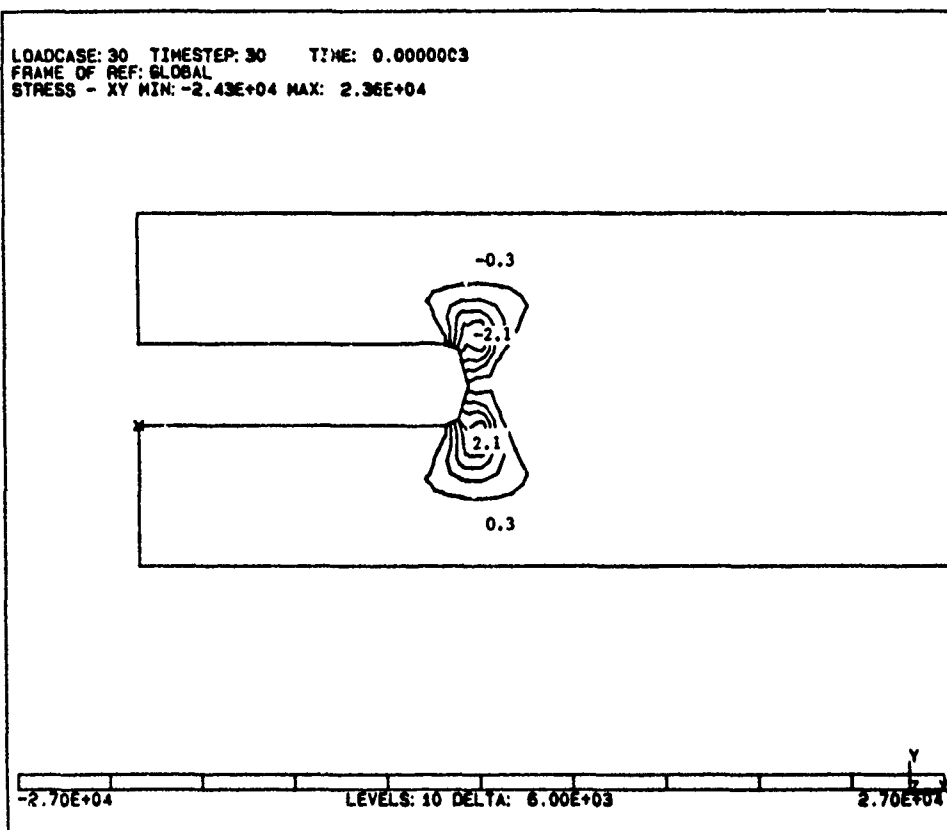
Figure 18. Shear Stress (t = 0.3 μs)

LOADCASE: 35 TIMESTEP: 35 TIME: 0.00000035
FRAME OF REF: GLOBAL
STRESS - XY MIN: -3.72E+04 MAX: 3.67E+04

-0.3
-2.7
2.7
0.3

-2.70E+04   LEVELS: 10 DELTA: 6.00E+03   2.70E+04
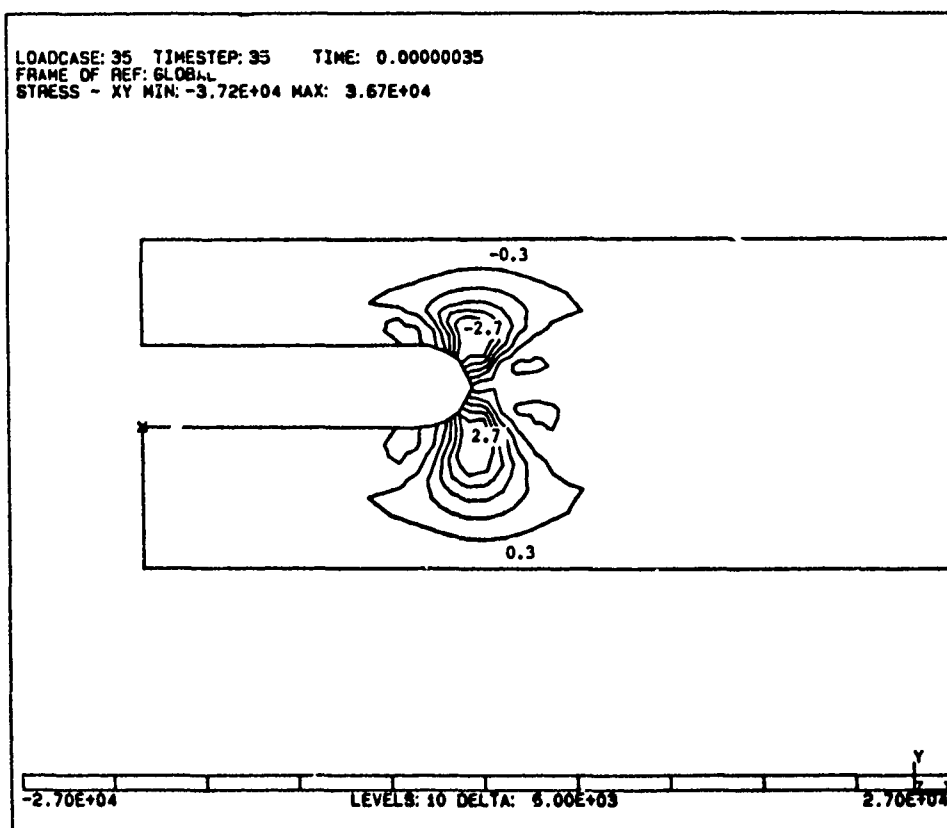
Figure 19. Shear Stress (t = 0.35 μs)

33

LOADCASE: 40 TIMESTEP: 40   TIME: 0.0000004
FRAME OF REF: GLOBAL
STRESS - XY MIN: -3.08E+04 MAX: 3.04E+04

-2.70E+04   LEVELS: 10 DELTA: 6.00E+03   2.70E+04

Figure 20. Shear Stress (t = 0.4 μs)

LOADCASE: 30 TIMESTEP: 30   TIME: 0.0000003
FRAME OF REF: GLOBAL
STRESS - X MIN: -4.59E+04 MAX: 3.46E+04

-4.50E+04   LEVELS: 10 DELTA: 1.00E+04   4.50E+04

Figure 21. Longitudinal Normal Stress (t = 0.3 μs)

34

LOADCASE: 35 TIMESTEP: 35   TIME: 0.00000035
FRAME OF REF: GLOBAL
STRESS - X MIN: -4.11E+04 MAX: 4.57E+04

-4.50E+04   LEVELS: 10 DELTA: 1.00E+04   4.50E+04

Figure 22. Longitudinal Normal Stress (t = 0.35 μs)

LOADCASE: 40 TIMESTEP: 40   TIME: 0.0000004
FRAME OF REF: GLOBAL
STRESS - X MIN: -3.55E+04 MAX: 3.73E+04

-4.50E+04   LEVELS: 10 DELTA: 1.00E+04   4.50E+04

Figure 23. Longitudinal Normal Stress (t = 0.4 μs)

35

4. SIMULATION OF THE STRESS WAVE INITIATION AND PROPOAGATION IN ONE DIMENSION

A number of finite difference solutions to the complete problem of energy deposition and subsequent motions were obtained. The code WONDY (Lawrence and Masur, 1971) (Refer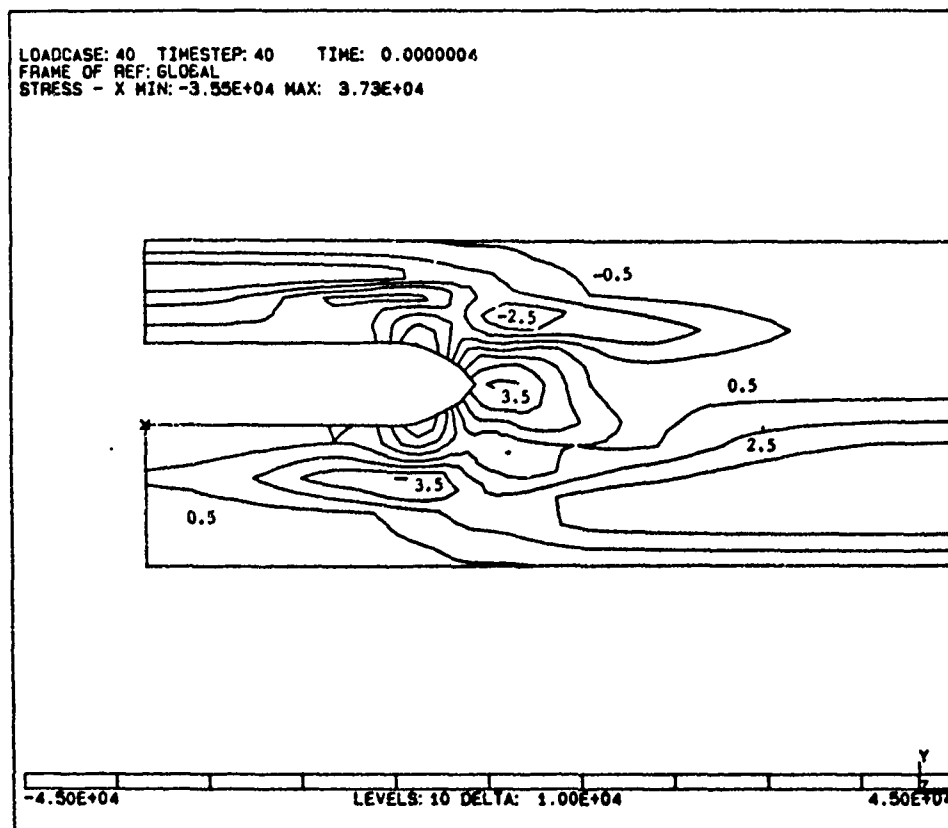ence 3) was utilized to obtain these results. A 20-layer composite laminate was divided into a total of 400 zones, with 20 zones in each layer. The total thickness was 0.1 inch, or 0.254 cm; each layer was then one-tenth of that thickness. The mass density of the material was 1.568 gm/cm^3, which is typical of an epoxy-graphite material (Froula et al., 1980) (Reference 2). The sound speed was $3.02x10^5$ cm/s (Lee, 1979) (Reference 4). A vapor transition was included; the vaporization energy was set at 10^{11} ergs/gm (Lee, 1979) (Reference 4).

For the solid region, a Mie-Grüneisen equation of state was used. The reference Grüneisen parameter was equal to 0.3 (Froula et al., 1980) (Reference 2). A linear wave speed versus particle velocity form was adopted, with a slope of 0.65 (Lee, 1979) (Reference 4). Thus, the material did not have a constant wave speed, but the model had nonlinearities.

For the stress deviator response, a linear elastic model with a von Mises plastic yield was used. The Poisson's ratio was 0.44 (Lee, 1979) (Reference 4), which gives a unaxial-strain wave speed of $3.26x10^5$ cm/s. Since the behavior for the initial energy deposition and subsequent wave motions is dominated by the hydrodynamic model, it was not necessary to use an anisotropic model for this part of the problem.

The yield stress was $0.5x10^9$ dynes/cm^2. Failure in tensile spall was assumed to occur at 10^9 dynes/cm^2 (14,500 psi).

With a longitudinal speed of $3.26x10^5$ cm/s, and a total thickness of 0.254 cm, the total plate transit time is $0.78x10^{-6}$ s, or just under a microsecond. The energy deposition time was set at one-fortieth of a microsecond, or $0.25x10^{-8}$ s. The energy was deposited at a constant rate over this time. For the spatial distribution, the linear shape discussed in the previous section was used as an approximation to the exponential shape characteristic of actual depositions. Thus, the maximum energy density occurred at the front surface, and that energy density decreased linearly to zero at a total depth of one-twentieth of the total thickness (0.0127 cm or 0.005 inch). The total flux was $2x10^8$ ergs/cm^2. With the deposition thickness of 0.0127 cm and the mass density of 1.568 gm, this gives an average initial energy density of 10^{10} ergs/gm. At the surface, the energy density is therefore $2x10^{10}$ ergs/gm.

36

Since the Grüneisen is 0.3, an instantaneous deposition of this energy would create an initial stress of $P = (1.568)(0.3)(2\times10^{10}) = 9.5\times10^{9}$ dynes/cm^2, or just under 10 kilobars, with a pulse width of 0.0127 cm. In fact, because of the finite deposition time, the actual pulse width is slightly higher, and the initial stress about half that value.

As discussed in Section 1.3, an initial triangular compressive pulse will generate a tensile following "tail" as it moves away from the free surface. As that tail builds in magnitude, tensile spall of the front surface will occur. Additional spall will occur until the final tensile magnitude decreased to under the spall strength of 1 kilobar.

Figure 24 shows the actual resultant wave at the time of 10^{-7} s, well after the final wave has moved away from the free front surface. The main compressive pulse is about 3 kilobars (40×10^{3} psi) at this time and is indeed almost triangular in shape. At times immediately after the energy deposition, parts of the front surface did spall as the tensile wave began to grow. Ultimately, a total thickness one-half the deposition depth was spalled. The tensile following wave, which was almost a kilobar at the time of final spall, has at this time decreased to about two-thirds of a kilobar.

This result illustrates the important effects of the material nonlinearities and especially the effects of the spall response. It is also worthwhile noting that, in this particular problem, the initial energy densities were below the vaporization energy (10^{11} ergs/gm) by a factor of 5. If the energy flux had been greater, the material near the free surface would have been vaporized, and the tensile strength would have decreased to zero.

The wave shown in Figure 24 propagates into the interior of the plate. Since the material is nonlinear, the stress pulse will decay in magnitude and broaden in width. For example, Figure 25 shows the resultant wave at the time of 0.7×10^{-6} s, just before it reaches the back free surface of the plate. At this time, the peak compressive wave has decayed to 30,000 psi, and the tensile portion has decayed to less than 6000 psi. The pulse is almost twice as wide as it was initially.
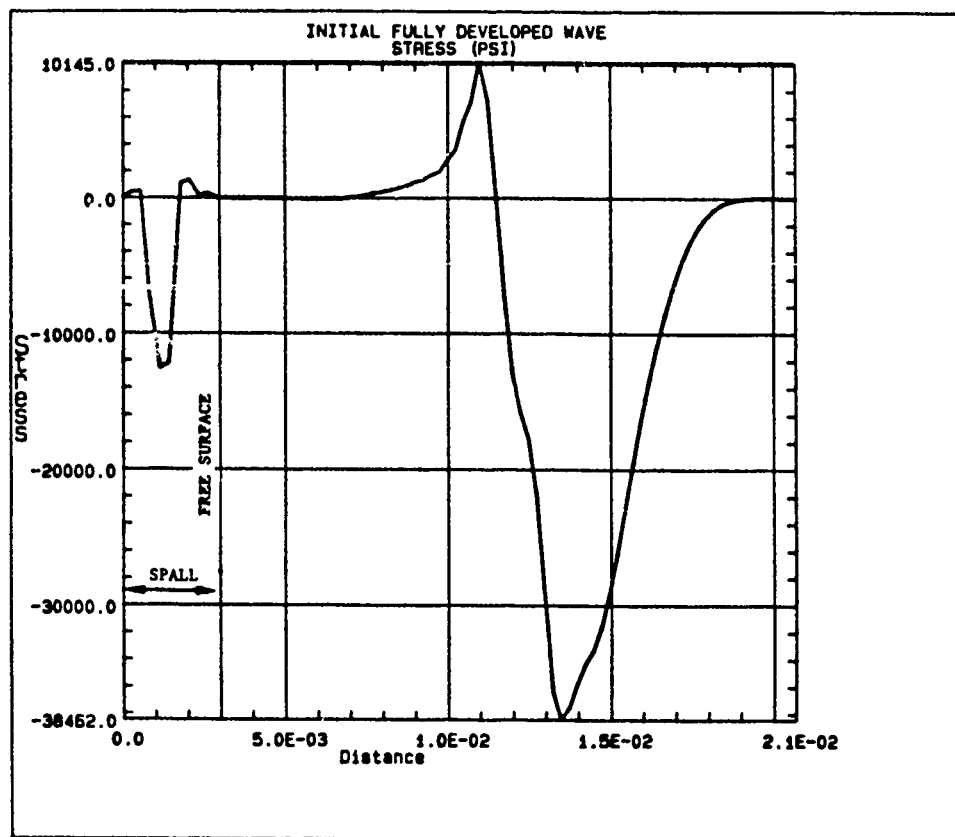
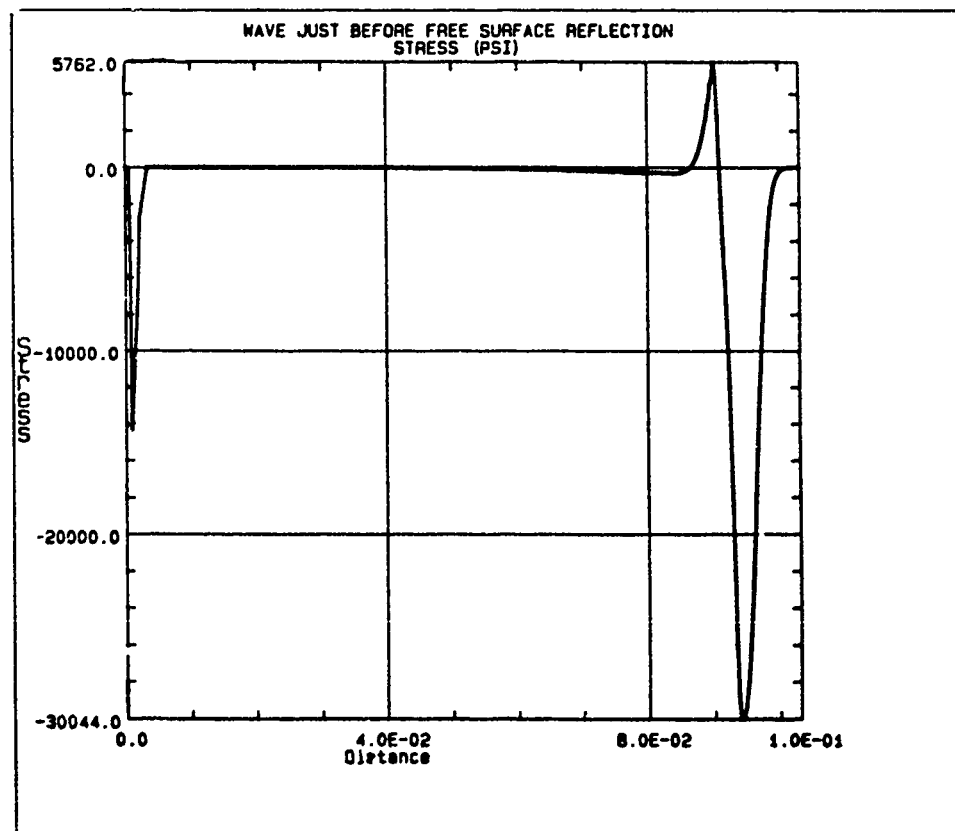Figure 24.   Initial Fully Developed Stress Wave (t = 0.1 µs)

Figure 25.   Stress Wave Just Before Free Surface Reflection (t = 0.7 µs)

38

5. SIMULATION OF THE STRESS WAVE INTERACTION WITH A DELAMINATION

As the stress wave reflects from the wall one would expect the surface plies to spall. To simulate such an event, we model the four plies adjacent to the surface. In the middle of these four plies is a small delamination with a half-length of 0.025 inch. The grid is the same as that used in the previous composite simulations (Figure 13), but the dimensions are reduced by half to give four elements per ply. The initial conditions are taken from the one-dimensional simulation at a time just before the reflection of the wave but just after the compressive part of the wave passes the delamination. The top and bottom surfaces are both considered stress-free. Since the stress wave lies ithin about two plies, the bottom surface observes essentially no stress from the time the compressive wave passes over until the time the reflected tensile wave returns. It is during this time frame that we have conducted a series of simulations varying the ply stacking sequence, plate temperature, crack geometry, and boundary restraints. Table 5 gives a summary of the test cases and the maximum fracture intensity values observed over each simulation. In the first six cases we vary the stacking sequence and observe that the maximum fracture parameters vary little from case to case. Even though the loading is not symmetric, the plates with delaminations between similiar plies show no mode II effects. Plates with delaminations between dissimilar plies show a small mode II effect, but still it is minor compared to a mode I fracture. The mode II strain energy release rate is especially small because the differential in the deformation tangent to the crack is small. Since the mode I strain energy release rate is defined primarily by the Young's modulus of the matrix, this parameter varies little with the ply sequence.

Wang et al. (1980) (Reference 12) found that, since the curing temperatures are so high (300°F), the thermal stress at room temperature is an important consideration when evaluating the strain energy release rate. To test this effect, in case 7, the plate is assumed to be 200°F colder than the reference temperature. In comparison to case 1, a significant change in the strain energy release rate is seen, indicating that the ambient temperature of the plate plays an important role in defining its fracture resistance. In this simulation, we assumed that the temperature of the plate suddenly dropped 200°F. This may give rise to some unwanted dynamical effects near the constrained regions of the plate. Since the delamination is removed from

Table 5. Dynamic Parametric Tests

case	ply sequence	comments	K_1 x10³ psi in	K_2 x10³ psi in	G_1 lb/in	G_2 lb/in	G lb/in
1	0/90/90/0		1.65	0.009	2.4	0	2.44
2	90/0/0/90		1.28	−0.004	2.31	0	2.31
3	0/0/90/90		1.36	−0.62	2.40	0.23	2.42
4	90/90/0/0		1.33	0.61	2.30	0.22	2.32
5	0/90/0/90		1.33	0.60	2.29	0.25	2.32
6	90/0/90/0		1.36	−0.61	2.40	0.26	2.43
7	0/90/90/0	cold plate	1.23	−0.062	1.44	0.01	1.45
8	0/90/90/9	edge delamination	1.65	−0.015	2.44	0	2.44
9	0/90/90/0	constrained	1.24	−0.73	1.38	0.15	1.53
10	90/90/0/0	constrained	0.998	−0.33	0.92	0.50	1.13
11	0/0/90/90	constrained	0.797	−0.10	1.38	0.17	1.55

these constraints, we expect that these effects are minor. In case 8, the delamination is assumed to reside on a free edge of the plate. Note that the fracture parameters changed very little. This is somewhat surprising since, in static tests, the edge delamination is much more apt to fracture.

The reason these dynamic tests do not show this behavior can again be attributed to the pulse wavelength to delamination length ratio. The tip of the delamination is initially unaware that the free surface is nearby. The free edge effects would be apparent only for delaminations on the order of the wavelength of the pulse.

In cases 9 through 11, the boundary is constrained so that only that portion of the boundary above the delamination is free. As the wave reflects off this back surface, a shear wave will ensue from the region near the constrained/unconstrained boundary. This shear wave propagates into the interior and interacts with the delamination to produce excessive stresses.

Since the shear wave is partially transmitted via the fibers, one would expect
to see variations in the fracture parameters depending on the stacking
sequence. The tests conducted verify this sensitivity. Since the shear waves
travel slower than the normal stress waves, the maximum value of the mode II
fracture parameters peak at a later time than the mode I parameters.

In all the simulations, the maximum fracture intensity conditions occurred
after the maximum of the tensile stress wave had passed slightly below the
crack and the compressive wave had partially reflected from the crack f·ee
surface. The critical strain energy release rate for unstable growth is still
in question, but under static loading tests Wang et al. (1980) (Reference 12)
quoted a value of 0.8 lb/in. This would imply that the spalling occurs well
before the maximum intensity conditions at a time just before the maximum
stress reaches the crack. In such a scenario, most of the energy would remain
as kinetic energy in a spall the size of which would be related to the stress
wavelength. This would effectively damp the wave in the main body by
preventing this energy from being converted to strain energy. The spall would
travel at a high rate of speed away from the main body. The velocity vector
plot in Figure 26 shows speeds on the order of 150 mph at the time of maximum
fracture intensity.

None of the simulations indicate that the initial tensile tail plays much
of a role in the fracture of the composite. This may not be true for loading
conditions other than the magnitude and profile assumed in the one-dimensional
simulations in Section 4.

Plots of the transverse normal and shear stress contours within the
singular element (0.0025 inch on edge) given in Figures 27 and 28 show a very
typical pattern. These plots are at a time of maximum fracture intensity. As
the wave interacts with the delamination, the region near the crack tip could
behave plastically. With this in mind, the contours of von Mises stress
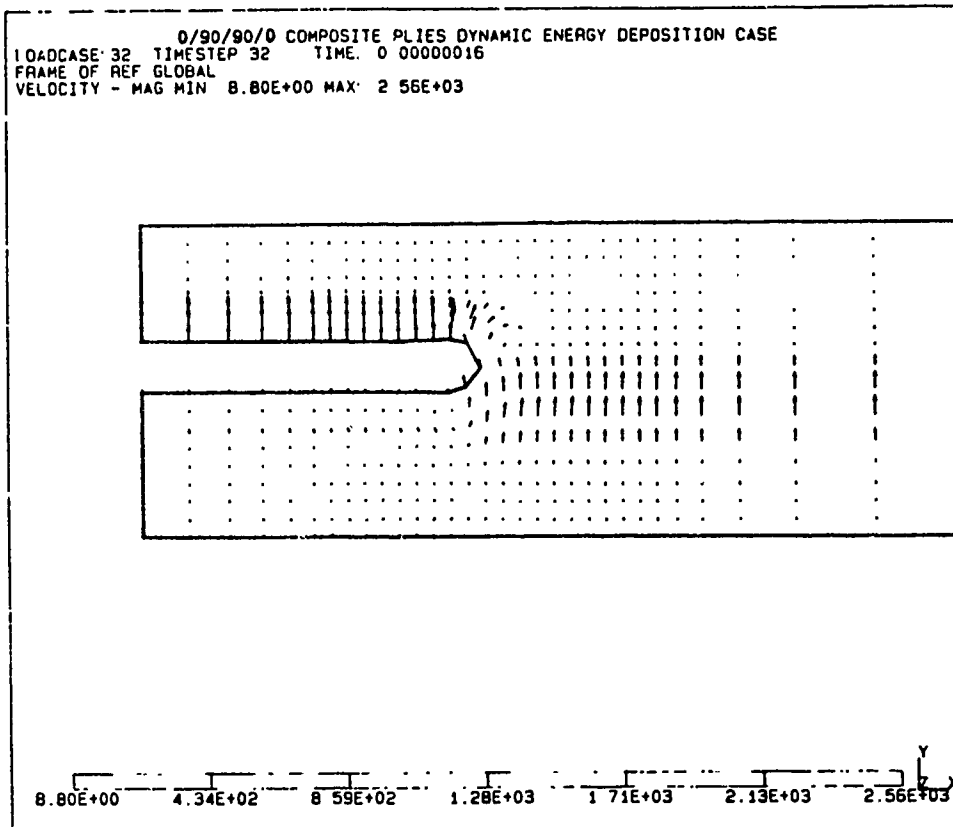plotted in Figure 29 give an indication of the size of the plastic region.

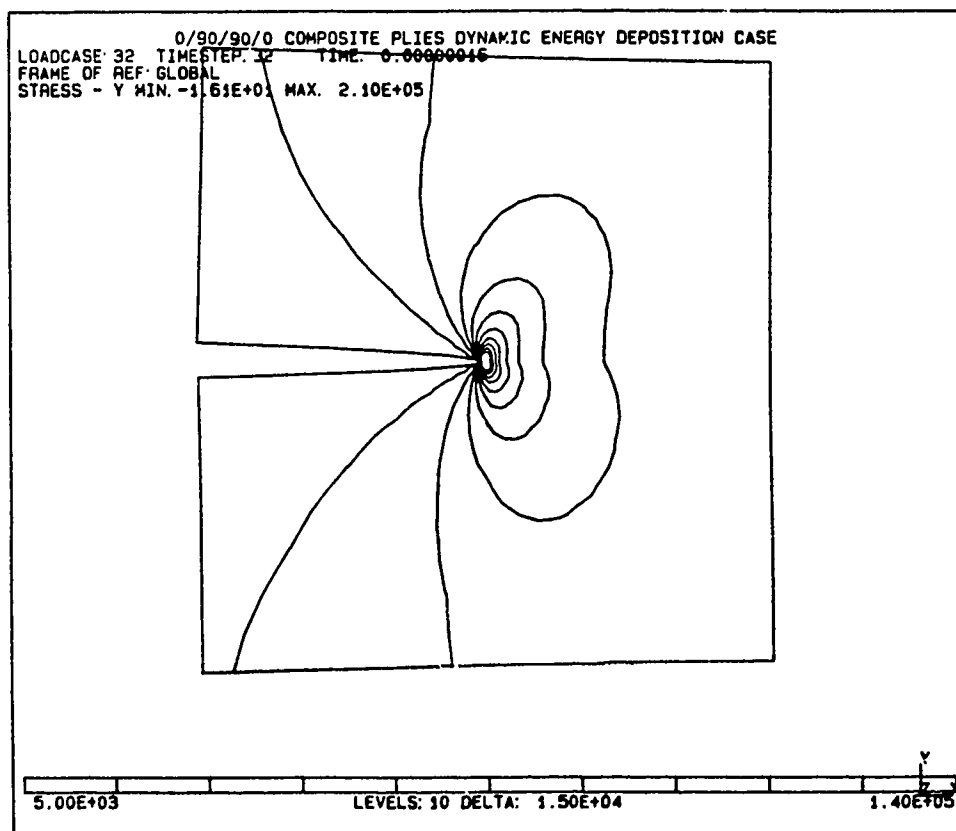Figure 26. Velocity Vector at Maximum Stress Intensity (t = 0.16 μs)

Figure 27. Normal Stress in the Singular Element (t = 0.16 μs)

42

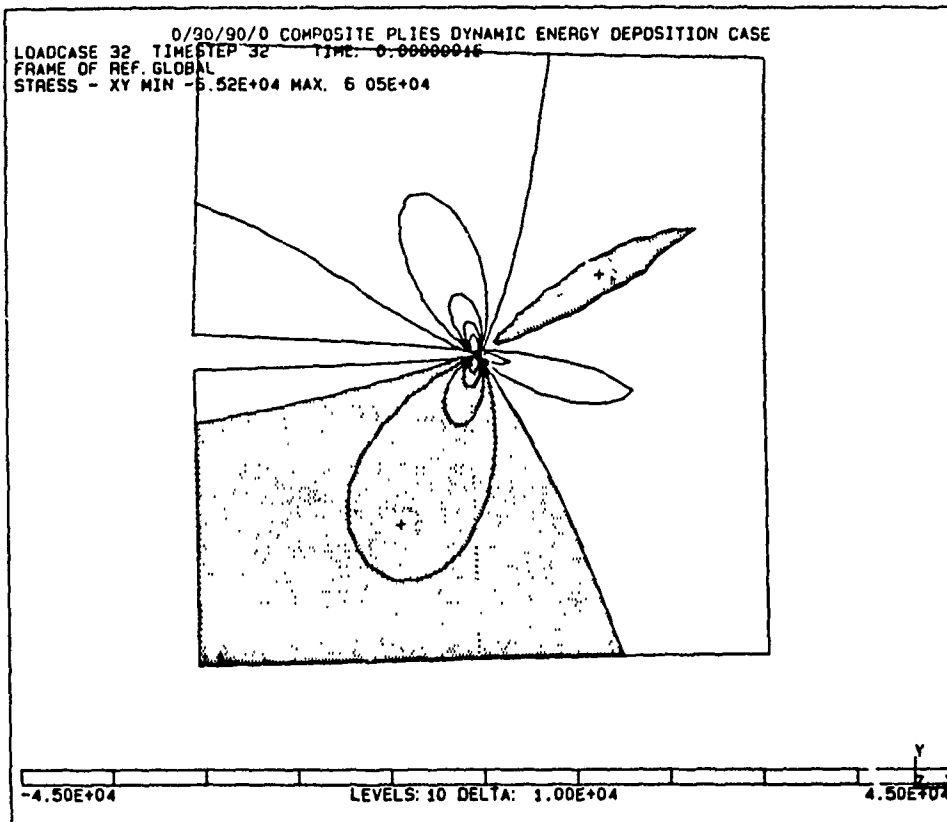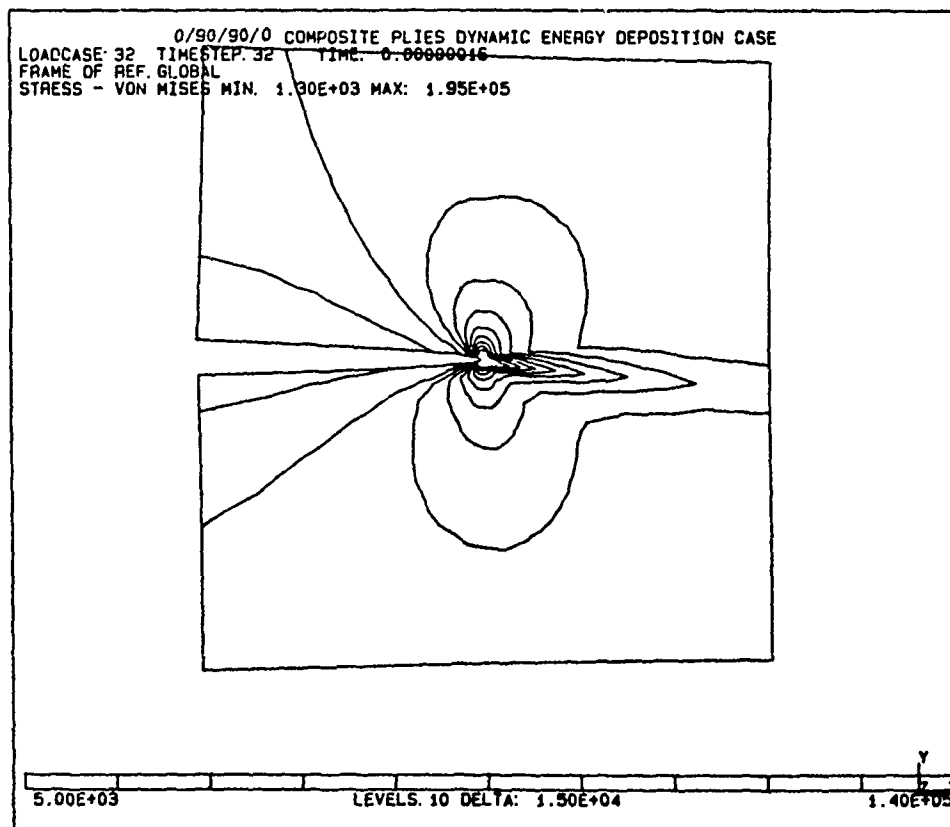Figure 28. Shear Stress in the Singular Element (t = 0.16 μs)

Figure 29. Von-Mises Stress in the Singular Element (t = 0.16 μs)

43

6. UNIFIED MODEL FEASIBILITY STUDY

The long-range goal of this study is the development of a complete finite element program for rapid thermal loading that is capable of an accurate and complete thermodynamic description similar to the finite difference code used in this study. As an interim measure we have used the finite difference model to describe the energy deposition aspects of the problem and to follow the resulting waves until they decay into the lower temperature solid behavior. At this level, a transfer to the finite element code is made to study the subsequent interaction with a pre-existing delamination. Such a treatment cannot, however, properly treat the coupling of the effects of the crack on the stress wave generation, which could be important for delaminations near the irradiated surface. In addition to these coupling effects, each of the individual models used in this Phase I study are inadequate, in certain respects, for describing the high-energy, high-stress behavior of the composite material. This is in part due to the lack of experimental data related to composites in this regime. Nevertheless, certain aspects could be improved with current knowledge. For example, in the current finite element model, the composite is treated as a linearly elastic anisotropic material. Certainly, as the plate is heated, an epoxy matrix would undergo some phase transition that alters its elastic properties, while the graphite fibers might retain their elastic properties at the same temperature. The result would be some anisotropic medium that behaves like a fluid in certain directions. Similarly, after the wave has moved out of the high-temperature region, the high stresses might cause the matrix to deform plastically.

Certain algorithmic features need to be employed to allow for more than one delamination, create new delaminations, and allow for partial or full closing of delaminations depending on the nature of the stress wave. The logic for closing delaminations may be conveniently expressed in the finite element context via Lagrangian multipliers. These multipliers represent the contact force between the sides of the delamination. In addition to interlaminar delaminations, the model should consider transverse cracks, which may be important when normal operating loads are also considered in the analysis.

In the current work, the stress wave generation was carried out in one dimension. This limits the analysis to the generation of longitudinal waves. The next step would be to carry out the analysis in two dimensions under plane stress/strain or axisymmetric assumptions. Strictly speaking, the anisotropic

44

and inhomogeneous properties of the composite plate rule out any assumptions of axisymmetry except in idealized cases. Similarly, plane stress/strain assumptions are applicable only by restricting the nature of the laser area deposition. The problem is truly three-dimensional, but the merit of three-dimensional calculations must be weighed with their complexity and the state of the art of the physical model. Three-dimensional simulations may be feasible under certain settings. Since the grid size must be related to the wavelength of the stress pulse, which is given by the laser pulse duration, short pulses imply fine grids. For the same amount of work, one might model long pulses over a large area, or short pulses over a small area.

Given that the physical models describing composites under extreme loading conditions are still in their infancy, it is absolutely imperative that the computer model be modular and structured. This will enable the model to evolve as experimental evidence and physical models become available. All the essential processes need to be at least identified early in the model development to form a framework to build on.

To this end, the finite element method offers just such a modular structure. Codes such as DYNA2D and DYNA3D, available in the public domain, are based on a finite element formulation, which includes finite deformation, large strain, and critical bulk viscosity to control shock waves. The codes include a mesh rezoner to maintain a proper mapping in these Langrangian calculations.

Unlike the FEAPICC codes, the formulation is explicit. This implies that no matrices need to be assembled or eliminated, reducing the computer time and memory. Since, for time accuracy, the step sizes must be set below the stability limit, the explicit formulation offers no drawbacks in this regard.

7. CONCLUSIONS

To summarize, we have addressed the problem of rapid deposition of thermal energy on the surface of a composite plate. Several general aspects of the problem have been described, and the assumptions regarding the analysis have been enumerated. Existing codes have been modified to solve the stress pulse generation and its subsequent interaction with a delamination within the composite plate. The finite difference model for simulation of the stress wave generation includes the thermomechanical coupling and a general equation of state model to account for phase changes. The finite element model accounts for the stress singularity of a delamination within the anisotropic composite plies. This model has been modified to include thermal stresses, to calculate the strain energy release rates, and to account properly for the plane strain assumptions. Tests have been conducted to ensure that the modifications have been implemented correctly and that the model is applicable to the problem we address.

Our analysis shows that the strain energy is a quadratic function of the mechanical and thermal loading with a strong coupling between the mechanical and thermal parts. While the study of Wang et al. (1980) (Reference 12) implies the contrary, the strain energy resulting from a combined mechanical and thermal load is not generally the sum of the strain energies of each load independently.

The results of the analysis of the stress wave generation indicate that the ensuing wave will have both compressive and tensile parts. The magnitude of the tensile part depends on the tensile strength or fracture toughness of the surface plies. As the wave propagates into the interior of the plate, the nonlinearities damp and spread this wave.

We have modeled, using the singular finite element method, the spalling event as the stress wave reflects from the back surface and interacts with an existing delamination. Our analysis indicates that the fracture parameters are insensitive to the stacking sequence when the delamination interacts with a pure tension wave. This is because the stress is transmitted primarily through the matrix. If a shear wave results from the loading or boundary constraints, then the stacking sequence has an appreciable effect on the fracture parameters, since the shear wave is transmitted via the fiber/matrix combination. The ambient temperature of the plate also proved to be an important consideration in the fracture, since the thermal deformation resulting from the curing of the composite can be significant.

46

There are many aspects of this model that need more attention. More experimental studies and models are needed to characterize the behavior of composites under extreme loads. We recommend that the models for stress generation and for its subsequent interaction with a delamination be unified under one finite element framework. The inherent modular structure of the FEM will lend itself to modifications as experimental data become available. Such a code could also help guide the experimental program and aid the experimentalists in interpreting their results.

REFERENCES

1. Aminpour, M. A. (1986) "Finite Element Analysis of Propagating Interface Cracks in Composites," Ph.D. Thesis, University of Washington, Dept. of Aeronautics and Astronautics.

2. Froula, N. H., Leikes, G. L., Stretanski, E. D., and Swick, M. K. (1980) "Grüneisen Parameter Measurements for Kevlar and Epoxy," Air Force Weapons Laboratory Report AFWL-TR-79-176, August.

3. Lawrence, R. J., and Masur, D. S. (1971) "Wondy IV - A Computer Program for One-Dimensional Wave Propagation with Rezoning," Sandia Laboratories Report SC-RR-71028, August.

4. Lee, L. M. (1979) "Graphite Resin Characterization Program for Nuclear Hardness Evaluation," Air Force Weapons Laboratory Report AFWL-TR-79-103.

5. Lin, K. Y., and Mar, J. W. (1976) "Finite Element Analysis of Stress Intensity Factors for Cracks at a Bi-material Interface," Int. J. of Fracture, Vol. 12, No. 4, August, pp. 521-531.

6. O'Leary, J. R. (1981) "An Error Analysis for Singular Finite Elements," TICOM Report 81-4, August.

7. Paramasivam, T., and Reismann, H. (1986) "Laser-Induced Thickness Stretch Motion of a Transversely Constrained Irradiated Slab," AIAA J., Vol. 24, No. 10, October, pp. 1650-55.

8. Rice, J. R., and Sih, G. C. (1965) "Plane Problems of Cracks in Dissimilar Media," J. Appl. Mech., June, pp. 418-423.

9. Stern, M. (1979) "Families of Consistent Conforming Elements with Singular Derivative Fields," Int. J. Num. Meth. in Eng., Vol. 14, pp. 409-421.

10. Tong, P., Pian, T. H. H., and Lasry, S. (1973) "A Hybrid Element Approach to Crack Problems in Plane Elasticity," Int. J. Num. Meth. in Eng., Vol. 7, pp. 297-308.

11. Walker, T., and Lin, K. Y. (1987) "A Singular Finite-Element Analysis of Interface Fracture in Composite Material," to be published.

12. Wang, A. S. D., Crossman, F. W., Law, G. E., and Warren, J. (1980) "A Comprehensive Study of Interlaminar and Intralaminar Fracture Growth in Composite Laminates," Annual Technical Report to AFOSR for Contract No. F49620-79-C-0206, Drexel University, November.